

Banner appropriate to article type will appear here in typeset article

Nusselt number scaling in horizontal convection

Navid C. Constantinou¹†, Cesar B. Rocha², Stefan G. Llewellyn Smith^{3, 4}, and William R. Young⁴

¹Research School of Earth Sciences & ARC Centre of Excellence for Climate Extremes, Australian National University, Canberra, ACT 2601, Australia

²Instituto Oceanográfico, Universidade de São Paulo, São Paulo, SP 05508-120, Brasil

³Department of Mechanical and Aerospace Engineering, University of California San Diego, La Jolla, CA 92093-0411, USA

⁴Scripps Institution of Oceanography, University of California San Diego, La Jolla, CA 92093-0213, USA

(Received xx; revised xx; accepted xx)

We report a numerical study of horizontal convection (HC) at Prandtl number $Pr = 1$, with both no-slip and free-slip boundary conditions. We obtain 2D and 3D solutions and determine the relation between the Rayleigh number Ra and the Nusselt number Nu . In 2D we vary Ra between 0 and 10^{14} . In the range $10^6 \lesssim Ra \lesssim 10^{10}$ the Nu - Ra relation is $Nu \sim Ra^{1/5}$. With Ra greater than about 10^{11} we find a 2D regime with $Nu \sim Ra^{1/4}$ over three decades, up to the highest 2D Ra . In 3D, with maximum $Ra = 10^{11.5}$, we find only $Nu \sim Ra^{1/5}$. These results apply to both free slip and no slip boundary conditions. The $Nu \sim Ra^{1/4}$ regime has a double boundary layer (BL): there is a thin BL with thickness $\sim Ra^{-1/4}$ nested inside a thicker BL with thickness $\sim Ra^{-1/5}$. The $Ra^{-1/4}$ BL thickness, which determines Nu , coincides with the Kolmogorov and Batchelor scales of HC.

Numerical and theoretical results indicate that 3D HC is qualitatively and quantitatively similar to 2D HC. At the same Ra , the 3D Nu exceeds the 2D Nu by less than 20%, i.e., there is very little 3D enhancement of heat transport. Boundary conditions are more important than dimensionality: the 2D free-slip solutions have larger Nu than 3D no-slip solutions. Using the mechanical energy power integral of HC we show that the mean square vorticity of 3D HC is nearly equal to that of 2D HC at the same Ra . Thus vorticity amplification by strain-mediated vortex stretching does not operate in 3D HC.

1. Introduction

Horizontal convection (HC) is convection driven by imposing non-uniform heating and cooling along a single horizontal surface, such as the top of a rectangular enclosure. There is no flux of heat through the other boundaries (Hughes & Griffiths 2008). Oceanography is an important motivation for consideration of HC (Sandström 1908; Rossby 1965; Coman *et al.* 2006), and in that connection the dependence of horizontal heat transport on the strength of buoyancy forcing applied at the ocean surface is a prime question. Buoyancy forcing is quantified via the horizontal-convective Rayleigh number, Ra , and horizontal heat transport by a suitably defined Nusselt number Nu (Rocha *et al.* 2020b).

† Email address for correspondence: navid.constantinou@anu.edu.au

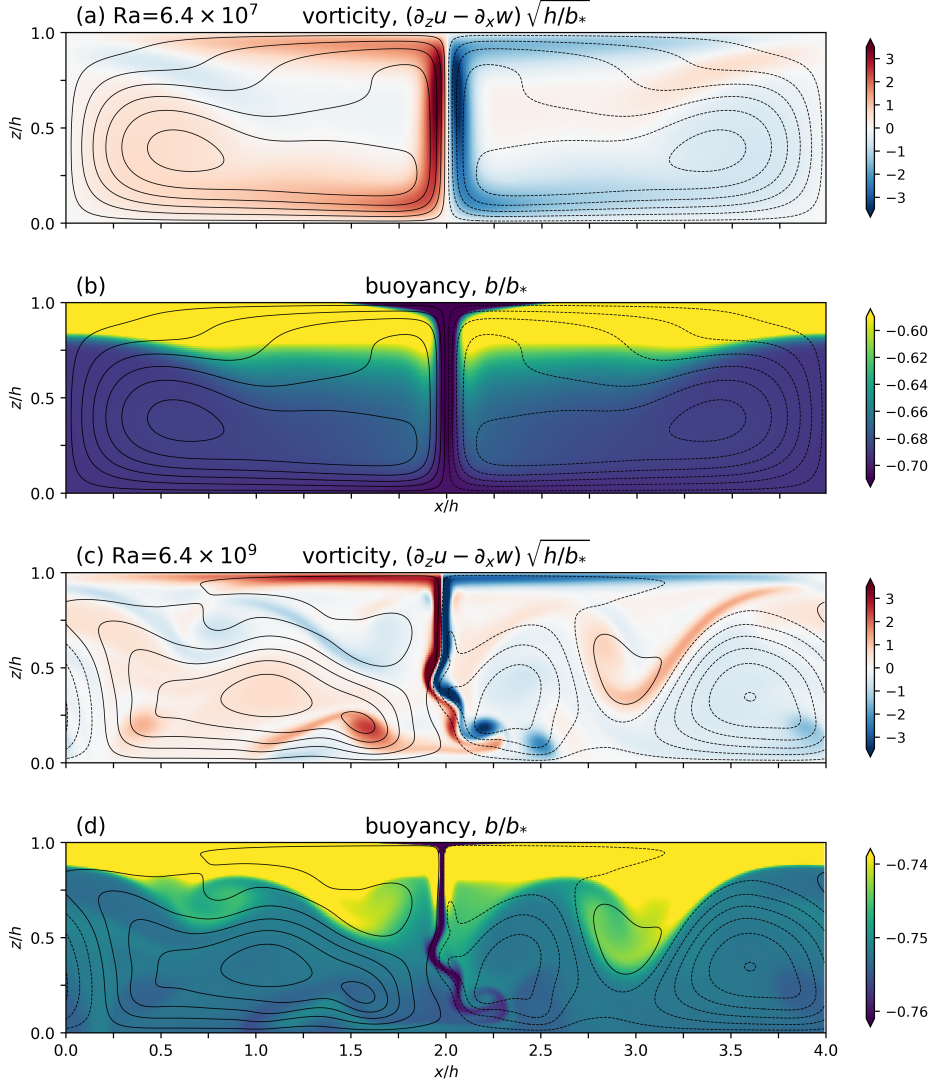


Figure 1: Snapshots of 2D free-slip (2DFS) HC at $\text{Ra} = 6.4 \times 10^7$ in panels (a) and (b) and $\text{Ra} = 6.4 \times 10^9$ in (c) and (d); $\text{Pr} = 1$. Contours are streamlines. At the top surface $-1 \leq b/b_* \leq +1$. The narrow range of the buoyancy color scale in (b) and (d) makes the very small interior buoyancy variations visible. The sinusoidal surface buoyancy in (2.4) defines the buoyancy scale b_* ; h is the layer depth.

HC is an interesting counterpoint to Rayleigh-Bénard convection because HC buoyancy transport in the interior of the domain cannot be easily interpreted as the vertical motion of thermal plumes. Instead, in HC heat enters the fluid where the non-uniform heated surface is hotter than average and exits where it is colder. This horizontal transport is associated with a prominent boundary layer (BL) adjacent to the non-uniform surface.

Citation	Pr	ℓ_x/h	max Ra	BC	forcing	p
Rossby (1998)	10	1	10^8	FS	linear	$\frac{1}{5}$
Siggers <i>et al.</i> (2004)	$\{\frac{1}{5}, \dots, 4\}$	1	$\approx 10^9$	FS	sin	$\frac{1}{5}$
Chiu-Webster <i>et al.</i> (2008)	∞	1	10^{10}	FS, NS	linear	$\frac{1}{5}$
Sheard & King (2011)	6.14	{1, 1.6, 6.25}	10^{12}	NS	linear	$\frac{1}{5}, >\frac{1}{5}$?
Ramme & Hansen (2019)	∞	1	10^{10}	FS	linear	$\frac{1}{5}$
	∞	1	10^{10}	FS	various	$\frac{1}{5}, \frac{1}{4}$?
Tsai <i>et al.</i> (2020)	6.14	6.25	$10^{12.5}$	NS	linear	$\frac{1}{5}, \frac{1}{4}$
	6.14	6.25	$10^{12.5}$	NS	various	$\frac{1}{5}$
This work	1	4	$10^{13.8}$	FS, NS	sin	$\frac{1}{5}, \frac{1}{4}$

Table 1: Summary of seven studies of Nu - Ra HC scaling using 2D direct numerical simulations. Prandtl number Pr is fixed at the values in column 2 and Ra is varied. In the final column p is the exponent in (1.2). The “forcing” column refers to the surface buoyancy profile $b_s(x)$: “linear” is $b_s(x) \propto x$; “sin” is sinusoidal; “various” is other $b_s(x)$ profiles. In the boundary condition (BC) column NS is no slip and FS is free slip. Siggers *et al.* (2004) used seven Pr ’s between 0.2 and 4. Sheard & King (2011) claim an elevation in p above 1/5 for $Ra \gtrsim 10^{10}$. Ramme & Hansen (2019) indicate that depending on the surface forcing profile $p = 1/4$ might be a better fit than $p = 1/5$ in the range $10^8 \lesssim Ra \leq 10^{10}$.

1.1. Rossby scaling

The oldest result for the high- Ra variation of horizontal-convective Nu is the scaling law of Rossby (1965),

$$Nu \sim Ra^{1/5} Pr^0, \quad (1.1)$$

where Pr is the Prandtl number. (Parameters Ra , Pr , and Nu are defined in section 2.) Rossby was motivated by experiments done using five values of Pr between 13 and 8 500. Rossby’s reasoning leading to (1.1) (reviewed in section 4) assumes visco-diffusive BL dynamics, justified by the assumption that $Pr \gg 1$.

“Rossby scaling” often means the exponent $p = 1/5$ in (1.1) without reference to Pr^0 and without mentioning Rossby’s requirement that $Pr \gg 1$. Rossby was aware of Pr^0 : in Rossby (1998) he demonstrated the weak dependence of Nu on Pr in the range $3 \leq Pr \leq 100$ (with fixed Ra ’s between 10^4 and 10^8). In view of alternative scaling laws discussed below, all of which have the form,

$$Nu \sim Ra^p Pr^q, \quad (1.2)$$

we reserve the term “Rossby scaling” for $(p, q) = (1/5, 0)$ with $Pr \gg 1$.

1.2. Non-Rossby scaling with $p = 1/5$

At moderately large Ra , the exponent $p = 1/5$ is supported by both laboratory work and numerical solutions (Rossby 1998; Mullarney *et al.* 2004; Siggers *et al.* 2004; Wang & Huang 2005; Chiu-Webster *et al.* 2008; Sheard & King 2011; Illicak & Vallis 2012). In tables 1 and 2

Citation	Pr	ℓ_x/h	ℓ_y/h	max Ra	BC	forcing	p
Gayen <i>et al.</i> (2014)	5	$6\frac{1}{4}$	$\frac{1}{4}$	$10^{11.8}$	NS	pwc	$\frac{1}{5}$
Reiter & Shishkina (2020)	{1, 10}	10	1	$10^{12.5}$	NS	pwc	$\frac{1}{4}, \frac{1}{5}, \approx \frac{1}{4}$
	$\frac{1}{10}$	10	1	$\sim 10^{11.7}$	NS	pwc	$\frac{1}{5}$
This work	1	4	1	$10^{11.5}$	FS, NS	sin	$\frac{1}{5}$

Table 2: Summary of three studies of Nu - Ra HC scaling using 3D direct numerical simulations. Prandtl number Pr is fixed at the values in column 2 and Ra is varied. In the final column p is exponent in (1.2). The “forcing” column refers to the surface buoyancy profile $b_s(x)$: “pwc” denotes a piecewise constant surface buoyancy profile and “sin” is the sinusoidal profile in (2.4).

we summarize various Nu - Ra scaling laws claimed on the basis of 2D and 3D numerical simulations of HC: $p = 1/5$ is the most common exponent of Ra .

The exponent $p = 1/5$ occurs so frequently, and in such different parameter settings, that the necessity of Rossby’s $Pr \gg 1$ scaling argument is questionable. For example, figure 1 shows two $Pr = 1$ numerical solutions both of which are in the same $p = 1/5$ scaling regime (see section 3). The $Pr = 0.1$ points in figure 2(a) of Reiter & Shishkina (2020) provide an example of $p = 1/5$ scaling in a case with $Pr \ll 1$.

Gayen *et al.* (2014) make the important point that the exponent $1/5$ also arises with a non-Rossby balance between inertia and buoyancy in the surface BL. This balance leads to the non-Rossby scaling

$$Nu \sim Ra^{1/5} Pr^{1/5}. \quad (1.3)$$

Shishkina *et al.* (2016) propose a $Pr \ll 1$ non-Rossby scaling argument resulting in

$$Nu \sim Ra^{1/5} Pr^{1/10}. \quad (1.4)$$

The scaling arguments leading to (1.1), (1.3) and (1.4) are reviewed in section 4 and put into a unified framework. The results in (1.3) and (1.4) may help explain the tenacity of $1/5$ as the primary exponent p in cases removed from Rossby’s $Pr \gg 1$ scenario.

1.3. Higher Ra and $p = 1/4$

At moderately large Ra , $10^8 \lesssim Ra \lesssim 10^{10}$, Tsai *et al.* (2020) find $p = 1/5$. But in the range $10^{10} \lesssim Ra \lesssim 10^{14}$, and provided that the imposed surface buoyancy varies linearly with the horizontal coordinate x , Tsai *et al.* (2020) report the scaling $p = 1/4$. In other words, as Ra increases at fixed Pr the primary exponent p in (1.2) increases from $1/5$ to $1/4$. In section 3 we report the same result: increasing Ra , with $Pr = 1$, results in an increase in p from $1/5$ to $1/4$. The solutions in figure 1 are in the $p = 1/5$ scaling regime while those in figure 2 are in the regime with $p = 1/4$. This increase in p with Ra is accompanied by a qualitative changes in the structure of HC. Comparing figure 2 with figure 1 there is a striking transition from laminar flow in figure 1 to 2D turbulence in figure 2. The axisymmetric vortices in figure 2 indicate that interior dynamics is close to that of a vortex gas characteristic of freely evolving unstratified 2D turbulence (McWilliams 1984, 1990; Benzi *et al.* 1987, 1988; Carnevale *et al.* 1991; Dritschel *et al.* 2008).

With one exception, the studies in tables 1 and 2 report that $p = 1/5$ is the first power-law scaling observed as Ra is increased from small values with fixed Pr (even with $Pr \leqslant 1$).

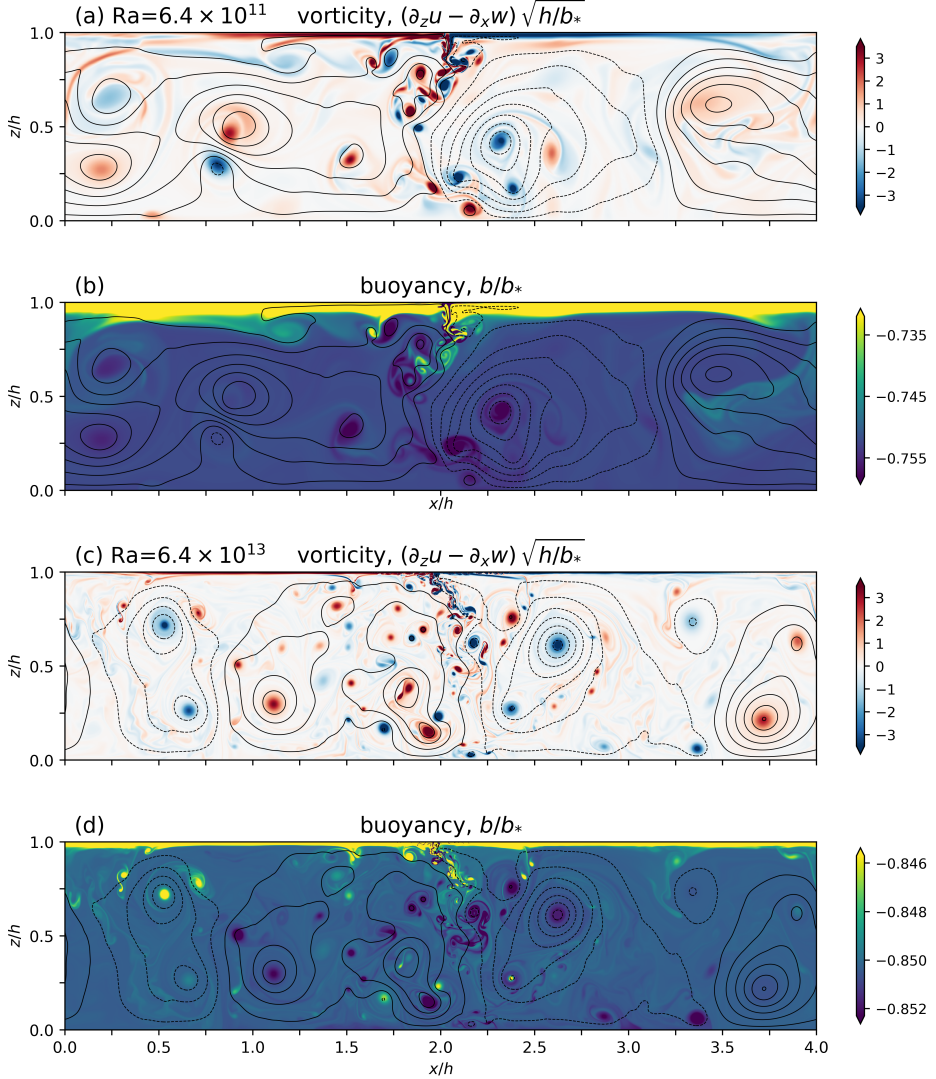


Figure 2: Snapshots of 2DFS solutions at $Ra = 6.4 \times 10^{11}$ in panels (a) and (b) and $Ra = 6.4 \times 10^{13}$ in (c) and (d); $Pr = 1$. Contours are streamlines. This illustration uses true aspect ratio so that axisymmetric vortices look circular. The buoyancy color scale is narrow in order to reveal the small interior buoyancy variations, which are localized within the cores of axisymmetric vortices. Across the six-decade range of Ra in figures 1 and 2 vorticity scales with $\sqrt{b_\star/h}$.

Based on [Tsai *et al.* \(2020\)](#), and our results in section 3, one might speculate that the first exponent $p = 1/5$ is, at sufficiently high Ra , replaced by $p = 1/4$. The exception, however, is the “complex scaling dependence” reported by [Reiter & Shishkina \(2020\)](#). With $Pr = 1$ and 10, and at relatively low Ra , [Reiter & Shishkina \(2020\)](#) report first a range with $p = 1/4$. As Ra is increased there is a transition to $p = 1/5$, followed at even higher Ra by second transition back to $p \approx 1/4$. The situation is further complicated because with $Pr = 0.1$ [Reiter & Shishkina \(2020\)](#) find only a single scaling regime with $p = 1/5$.

Three-dimensionality distinguishes [Reiter & Shishkina \(2020\)](#) from the 2D studies in table 1. But the comparable 3D study by [Gayen *et al.* \(2014\)](#) finds only $p = 1/5$ regimes. In

the 3D solutions reported below we also find only $p = 1/5$ regimes. The computations of Reiter & Shishkina (2020) reach the highest values of Ra in 3D HC reported in the literature. But the differences summarized above are at moderate values of Ra where there are several decades of overlap with other studies of HC (including this one). The most striking difference of Reiter & Shishkina (2020) from other work summarized in tables 1 and 2 is that with $Pr = 1$ and 10, the exponent $p = 1/4$ is the first exponent encountered as Ra is increased from small values. The piecewise constant buoyancy profile used as a surface boundary condition might be responsible for the distinctive Ra - Nu scaling reported by Reiter & Shishkina (2020).

In support of the hypothesis that the surface boundary condition might affect p , the 2D $Pr = \infty$ study of Ramme & Hansen (2019) shows a transition from steady to unsteady flow at $Ra \approx 10^8$. In the case of a piecewise constant buoyancy profile (but not with a linear surface buoyancy profile) this transition is accompanied by an increase in p from $1/5$ to $\approx 1/4$. Note, however, that consistent of Rossby (1965), and with Chiu-Webster *et al.* (2008), Ramme & Hansen (2019) do find that $p = 1/5$ as the first exponent encountered as Ra is increased from small values.

In section 2 we formulate the horizontal convection problem. Section 3 is a numerical study of HC in which we vary Ra at $Pr = 1$. All solutions use the sinusoidal surface buoyancy profile in (2.4). There are four solution suites corresponding to no-slip and free-slip boundary conditions and to 2D and 3D solutions. Section 4 is a review of various Ra - Nu scaling arguments leading to $p = 1/5$. Using the mechanical energy power-integral of HC we put these arguments into a unified framework. Section 4 also shows that the $p = 1/4$ scaling regime is characterized by a “double boundary layer”: there is a thin BL, with thickness $\sim Ra^{-1/4}$, nested inside a wider BL with thickness $\sim Ra^{-1/5}$. Section 5 provides further characterization of the double BL structure of the $p = 1/4$ scaling regime. Section 6 shows that the exponent $p = 1/4$ follows from the assumption that the thickness of the inner BL is determined by the Kolmogorov and Batchelor length scales of HC. In section 7 we show that vorticity amplification by strain mediated vortex stretching does not operate in 3D HC: as $Ra \rightarrow \infty$ the mean-square vorticity in 2D and 3D solutions are almost the same. Section 8 concludes.

2. Formulation of the horizontal convection problem

We consider a Boussinesq fluid with density $\rho = \rho_0(1 - g^{-1}b)$, where ρ_0 is a constant reference density and b is the “buoyancy”. If, for example, the fluid is stratified by temperature variations then $b = g\alpha(T - T_0)$, where T_0 is a reference temperature and α is the thermal expansion coefficient. The Boussinesq equations of motion are

$$\mathbf{u}_t + \mathbf{u} \cdot \nabla \mathbf{u} + \nabla p = b\hat{\mathbf{z}} + \nu \nabla^2 \mathbf{u}, \quad (2.1)$$

$$b_t + \mathbf{u} \cdot \nabla b = \kappa \nabla^2 b, \quad (2.2)$$

$$\nabla \cdot \mathbf{u} = 0. \quad (2.3)$$

The kinematic viscosity is ν and the thermal diffusivity is κ .

2.1. Horizontal convective boundary conditions and control parameters

We suppose the fluid occupies a domain with depth h , length ℓ_x , width ℓ_y ; we assume periodicity in the x - and y -directions. At the bottom surface ($z = 0$) and top surface ($z = h$) the primary boundary conditions on the velocity, $\mathbf{u} = (u, v, w)$, is that $w = 0$; the viscous boundary condition is either no slip (NS), $u = v = 0$, or free slip (FS), $u_z = v_z = 0$. At the bottom $z = 0$ the buoyancy boundary condition is no flux, $\kappa b_z = 0$. At the top, $z = h$, the boundary condition is $b = b_s(x)$, where the top surface buoyancy b_s is a prescribed function

of x . As a surface buoyancy field we use

$$b_s(x) = b_\star \cos kx, \quad (2.4)$$

where $k = 2\pi/\ell_x$.

As an idealization of conditions at the sea surface, FS is better than NS. But the main reason for considering different viscous boundary conditions is to test scaling arguments. We find only minor quantitative differences in the *Nu–Ra* scaling between the two boundary conditions. In the numerical solutions described below the main features of the *Nu–Ra* scaling relation are independent of the viscous boundary condition.

The problem is characterized by four non-dimensional parameters: the Rayleigh and Prandtl numbers

$$Ra \stackrel{\text{def}}{=} \frac{\ell_x^3 b_\star}{\nu \kappa}, \quad \text{and} \quad Pr \stackrel{\text{def}}{=} \frac{\nu}{\kappa}, \quad (2.5)$$

and the aspect ratios ℓ_x/h and ℓ_y/h . With periodic boundary conditions in y (no side walls), 2D HC is the special case $\ell_y/h = 0$. The Rayleigh number in (2.5) is defined using the amplitude b_\star of the sinusoid in (2.4). Other authors use the total difference (peak-to-trough) in buoyancy to define Ra . For comparison one might multiply our numerical values of Ra in section 3 by two.

2.2. Mechanical energy dissipation

We use an overbar to denote an average over x , y , and t , taken at any fixed z and angle brackets $\langle \rangle$ to denote a total volume average over x , y , z , and t . Using this notation, we recall some results from Paparella & Young (2002) that are used below.

Horizontally averaging the buoyancy equation (2.2) we obtain the zero-flux constraint

$$\overline{wb} - \kappa \bar{b}_z = 0. \quad (2.6)$$

Taking $\langle \mathbf{u} \cdot (2.1) \rangle$, we obtain the kinetic energy power integral

$$\varepsilon = \langle wb \rangle, \quad (2.7)$$

where $\varepsilon \stackrel{\text{def}}{=} \nu \langle |\nabla \mathbf{u}|^2 \rangle$ is the rate of dissipation of kinetic energy and $\langle wb \rangle$ is rate of conversion between potential and kinetic energy.

Vertically integrating (2.6) from $z = 0$ to h , and using $\overline{b_s(x)} = 0$, we obtain another expression for $\langle wb \rangle$. Substituting this into (2.7)

$$\varepsilon = -\frac{\kappa \bar{b}(0)}{h}. \quad (2.8)$$

In (2.8), $\bar{b}(0)$ is the (x, y, t) -average of the buoyancy at the bottom $z = 0$.

2.3. The Nusselt number of horizontal convection

Following Rocha *et al.* (2020b), we use the dissipation of buoyancy variance,

$$\chi \stackrel{\text{def}}{=} \kappa \langle |\nabla b|^2 \rangle, \quad (2.9)$$

to define the Nusselt number as

$$Nu \stackrel{\text{def}}{=} \chi / \chi_{\text{diff}}. \quad (2.10)$$

Above, $\chi_{\text{diff}} \stackrel{\text{def}}{=} \kappa \langle |\nabla b_{\text{diff}}|^2 \rangle$ is the buoyancy dissipation of the diffusive solution, i.e., $\kappa \nabla^2 b_{\text{diff}} = 0$ with b_{diff} satisfying the same boundary conditions as b .

Application of variational methods to HC (Siggers *et al.* 2004; Winters & Young 2009;

Rocha *et al.* 2020a) results in bounds on χ taking the form $Nu \lesssim Ra^{1/3}$. The exponent 1/3 is safely larger than the exponents 1/5 and 1/4 reported in numerical studies of HC, including this work.

Rocha *et al.* (2020b) show that there is also a “surface Nusselt number”

$$Nu_s \stackrel{\text{def}}{=} \overline{b_s \kappa b_z(h)} / \overline{b_s \kappa b_{\text{diff}}(h)}. \quad (2.11)$$

Above, $\kappa b_z(h)$ is the buoyancy flux through the top surface $z = h$. With sufficient temporal averaging $Nu = Nu_s$. The interior entropy production, χ , is balanced by an entropy flux through the surface $z = h$. Nu_s is the non-dimensional entropy flux though the surface. In numerical solutions described below, in which the temporal average is computed over a finite time interval, $Nu \approx Nu_s$ is a check on the estimated Nusselt number.

3. A numerical study of horizontal convection with $Pr = 1$

In this section we present the results of a numerical study directed at characterizing the variation of the Nusselt number Nu in (2.10) as a function of Ra . Computations are performed using Dedalus, a spectral framework for solving partial differential equations (Burns *et al.* 2020, www.dedalus-project.org). We use Fourier bases in the horizontal, periodic directions and a Chebyshev basis in the vertical; the equations are time stepped using a fourth-order implicit-explicit Runge–Kutta scheme.

We limit attention to $Pr = 1$ and the sinusoidal surface buoyancy forcing $b_s(x)$ in (2.4). We discuss both **NS** and **FS** boundary conditions and consider 2D solutions with aspect ratios

$$\ell_x/h = 4, \quad \ell_y/h = 0, \quad (3.1)$$

and 3D solutions with

$$\ell_x/h = 4, \quad \ell_y/h = 1. \quad (3.2)$$

Thus we have four solution suites: **2DFS**, **3DFS**, **2DNS**, and **3DNS**. The estimates of Nu are summarized in table 3 and figure 3.

3.1. The low- Ra regime

Analysis of the low- Ra regime in appendix A shows that with $\ell_x/h = 4$ the first variation of the Nusselt number away from unity is

$$Nu^{\text{FS}} = 1 + \left(\frac{Ra}{21567.5} \right)^2 + \text{ord}(Ra^4), \quad (3.3)$$

and

$$Nu^{\text{NS}} = 1 + \left(\frac{Ra}{87789.8} \right)^2 + \text{ord}(Ra^4). \quad (3.4)$$

The low- Ra regime means that the Ra^2 term in (3.3) and (3.4) is less than one, i.e., that the convective buoyancy transport is a weak enhancement of the diffusive transport. For **FS** low Ra means that Ra is somewhat less than about 2.5×10^3 and for **NS** low Ra means that Ra is somewhat less than about 10^4 . These analytic results are compared with numerical solutions in the insert of figure 3. For example, the **2DFS** solution at $Ra = 6.4$ has $Nu - 1 = 8.8 \times 10^{-8}$ and at $Ra = 640$, $Nu - 1 = 8.8 \times 10^{-4}$. The approximations in (3.3) and (3.4) are very accurate for $Ra < 10^3$. Table 3 does not include these very low- Ra results.

Ra	Free-slip Nu		No-slip Nu		Highest resolution n_x, n_z
	2D \circ	3D \bullet	2D \square	3D \blacksquare	
1.28e03	1.00	1.00 [†]	1.00	1.00 [†]	128, 32
3.20e03	1.02	1.02 [†]	1.00	1.00 [†]	128, 32
4.48e03	1.04	1.04 [†]	1.00	1.00 [†]	128, 32
6.40e03	1.08	1.08 [†]	1.01	1.01 [†]	128, 32
1.28e04	1.22	1.22 [†]	1.02	1.02 [†]	128, 32
1.92e04	1.38	1.38 [†]	1.04	1.04 [†]	128, 32
3.20e04	1.64	1.64 [†]	1.11	1.11 [†]	128, 32
6.40e04	2.07	2.07 [†]	1.28	1.28 [†]	128, 32
1.28e05	2.55	2.55 [†]	1.59	1.59 [†]	128, 32
2.56e05	3.04	3.04 [†]	1.96	1.96 [†]	128, 32
6.40e05	3.71	3.71 [†]	2.47	2.47 [†]	128, 32
1.60e06	4.50	4.50 [†]	3.01	3.01 [†]	256, 64
3.20e06	5.14	5.14 [†]	3.45	3.45 [†]	256, 64
6.40e06	5.80	5.80 [†]	3.93	3.93 [†]	256, 64
1.60e07	6.77	6.77 [†]	4.70	4.70 [†]	256, 64
3.20e07	7.61	7.61 [†]	5.38	5.44 [#]	256, 64
6.40e07	8.65	8.68*	6.17	6.59 [#]	256, 64
1.60e08	10.48	10.57*	7.41	8.46 [#]	256, 64
3.20e08	12.17*	12.19*	8.51	10.11 [#]	256, 64
6.40e08	14.01*	14.09*	9.69	11.97*	256, 64
1.60e09	16.99*	17.07*	11.77*	14.75*	256, 64
3.20e09	19.60*	20.32*	13.53*	17.20*	512, 128
6.40e09	22.41*	24.64*	15.35*	19.86*	512, 128
1.60e10	27.32*	31.38*	18.83*	23.67*	512, 128
3.20e10	31.48*	37.28*	21.88*	27.61*	512, 128
6.40e10	36.08*	43.94*	25.50*	30.68*	512, 128
1.28e11	41.85*	49.74*	29.87*	36.67*	1024, 256
1.60e11	43.80*		32.02*		1024, 256
3.20e11	50.71*	59.91*	37.45*	44.01*	1024, 256
6.40e11	58.36*		44.23*		1024, 256
1.60e12	71.43*		55.65*		1024, 256
3.20e12	86.26*		66.97*		2048, 512
6.40e12	101.32*		78.86*		4096, 1024
1.60e13	128.44*		97.66*		4096, 1024
6.40e13	178.55*		133.16*		4096, 1024

Table 3: Nu - Ra data for HC DNS. All runs have $Pr = 1$ and $\ell_x/h = 4$. 3D runs have $\ell_y/h = 1$ and $n_y = n_z$. The surface buoyancy is the sinusoid in (2.4). Unsteady solutions are indicated by a superscript * on Nu ; strictly 2D solutions (no y -dependence and $v = 0$) of 3D computations are marked by a superscript †. The four NS runs with superscript # are 3D but steady.

3.2. Nu - Ra scaling regimes: $p = 1/5$ and $p = 1/4$

Between $Ra \sim 10^4$ and 10^5 we do not see a simple relation between Nu and Ra . But once Ra is greater than about 6.4×10^5 we find the $p = 1/5$ scaling,

$$Nu \sim K_{1/5} Ra^{1/5}, \quad (3.5)$$

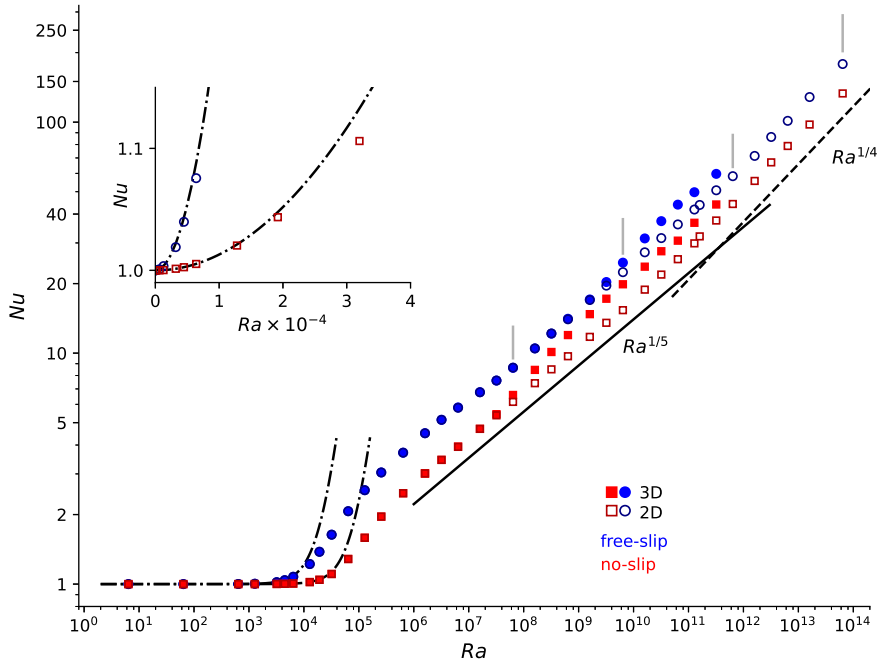


Figure 3: Variation of Nusselt number Nu with Rayleigh number Ra using the data from table 3. The inset compares the low- Ra numerical results with the low- Ra analytic results (3.3) and (3.4). Some solid markers fall on top of open markers, indicating that the 3D solutions evolve to become 2D, or that the three dimensionality is weak. The four vertical grey line segments mark Ra 's of the solutions in figures 1 and 2.

in all four solution suites. Starting at around $Ra \sim 10^{11}$ in the 2DNS suite, and 10^{12} in the 2DFS suite, there is a transition from the regime (3.5) to the $p = 1/4$ scaling

$$Nu \sim K_{1/4} Ra^{1/4}. \quad (3.6)$$

The $p = 1/4$ regime with NS has been reported previously by Tsai *et al.* (2020).

In figure 4 we show the data from figure 3, replotted using the compensated Nusselt number $Ra^{-1/5}Nu$ in panel (a) and $Ra^{-1/4}Nu$ in panel (b). Table 4 summarizes the exponents determined by least-squares fitting the Ra - Nu data over selected ranges. Least-squares exponents are broadly in agreement with the scaling regimes determined by visual inspection of figure 4 and other compensated plots. We use least-squares because it is objective and reproducible. Least squares also assesses the sensitivity of estimated exponents to the points at the beginning and end of a putative scaling range.

3.3. Discussion of the no-slip solutions

We begin with the 2DNS solution suite. The $p = 1/5$ scaling (3.5) is found across the four-decade range in row 1 of table 4. This is the plateau at $K_{1/5} = 0.17$ in figure 4(a). Least-squares estimates of exponent and prefactor, $K_{1/5}$, are robust to changes in the range, e.g., row 2 of table 4. The 2DNS suite transitions to the $p = 1/4$ scaling (3.6) at around $Ra = 10^{11}$ and forms the plateau at $K_{1/4} = 0.05$ in figure 4(b); see rows 4 through 6 of table 4.

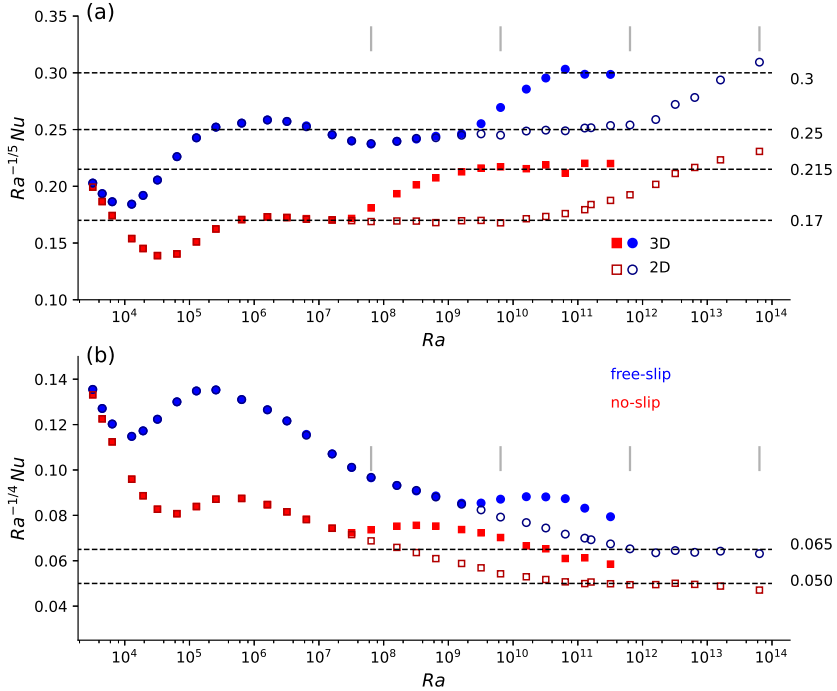


Figure 4: Variation of “compensated Nusselt numbers” (a) $Ra^{-1/5} Nu$ and (b) $Ra^{-1/4} Nu$ with Rayleigh number Ra . The four vertical grey line segments mark Ra ’s of the solutions in figures 1 and 2.

The **3DNS** solution suite is more complicated. With moderate Ra (rows 7 through 9 of table 4) the **3DNS** solutions coincide with their **2DNS** partners and the scaling is again (3.5) with $K_{1/5} = 0.17$. At a critical Ra of roughly 3.2×10^7 the **3DNS** suite becomes unstable to 3D perturbations. With further increases in Ra the **3DNS** solutions have larger Nu than their **2DNS** colleagues: the four steady **3DNS** solutions in the interval $3.20 \times 10^7 \leq Ra \leq 3.20 \times 10^8$, are here. One might expect that development of 3D flow, albeit steady 3D flow, signals the beginning of a new scaling regime, with an exponent p greater than $1/5$. But alas, this is the transition discovered by [Gayen et al. \(2014\)](#): at about $Ra = 1.60 \times 10^9$ the **3DNS** solutions enter a new $p = 1/5$ regime: see rows 10 through 12 of table 4 and the **3DNS** plateau at 0.215 in figure 4(a). With maximum $Ra = 3.20 \times 10^{11}$, we did not find convincing evidence of $p = 1/4$ in the **3DNS** solution suite.

The **NS** computations of [Gayen et al. \(2014\)](#) used $Pr = 5$ and a piecewise constant surface buoyancy. Instead of (2.10), [Gayen et al. \(2014\)](#) defined Nu based on the buoyancy flux through the destabilized portion of the non-uniformly heated surface. Despite these differences, [Gayen et al. \(2014\)](#) document analogous **3DNS** behavior involving two $p = 1/5$ scaling regimes: the constant $K_{1/5}$ takes different values on either side of a smooth transition. In the second $p = 1/5$ regime the results of [Gayen et al. \(2014\)](#) are based on large eddy simulation (LES). But our direct numerical solutions also reenter the $p = 1/5$ regime. Reentry to $p = 1/5$ cannot be dismissed as an artifact of LES.

row	suite	range	points	least squares Nu
1	2DNS	$6.40 \times 10^5 \leq Ra \leq 6.40 \times 10^9$	13	$0.177 Ra^{0.198}$
2	2DNS	$1.60 \times 10^6 \leq Ra \leq 3.20 \times 10^9$	11	$0.178 Ra^{0.197}$
4	2DNS	$6.40 \times 10^{10} \leq Ra \leq 6.40 \times 10^{13}$	10	$0.062 Ra^{0.242}$
5	2DNS	$6.40 \times 10^{10} \leq Ra \leq 1.60 \times 10^{13}$	9	$0.056 Ra^{0.246}$
6	2DNS	$1.28 \times 10^{11} \leq Ra \leq 1.60 \times 10^{13}$	8	$0.055 Ra^{0.246}$
7	3DNS	$6.40 \times 10^5 \leq Ra \leq 3.20 \times 10^7$	6	$0.173 Ra^{0.199}$
8	3DNS	$6.40 \times 10^5 \leq Ra \leq 6.40 \times 10^6$	4	$0.167 Ra^{0.202}$
9	3DNS	$3.20 \times 10^6 \leq Ra \leq 3.20 \times 10^7$	4	$0.179 Ra^{0.197}$
10	3DNS	$1.60 \times 10^9 \leq Ra \leq 3.20 \times 10^{11}$	8	$0.195 Ra^{0.204}$
11	3DNS	$1.60 \times 10^9 \leq Ra \leq 1.60 \times 10^{10}$	4	$0.191 Ra^{0.205}$
12	3DNS	$3.20 \times 10^{10} \leq Ra \leq 3.20 \times 10^{11}$	4	$0.180 Ra^{0.208}$
20	2DFS	$6.40 \times 10^5 \leq Ra \leq 1.60 \times 10^{11}$	18	$0.253 Ra^{0.199}$
21	2DFS	$6.40 \times 10^5 \leq Ra \leq 3.20 \times 10^8$	9	$0.312 Ra^{0.186}$
22	2DFS	$6.40 \times 10^8 \leq Ra \leq 1.60 \times 10^{11}$	9	$0.215 Ra^{0.206}$
23	2DFS	$6.40 \times 10^{11} \leq Ra \leq 6.40 \times 10^{13}$	6	$0.074 Ra^{0.245}$
24	2DFS	$6.40 \times 10^{11} \leq Ra \leq 3.20 \times 10^{12}$	3	$0.082 Ra^{0.241}$
25	2DFS	$6.40 \times 10^{12} \leq Ra \leq 6.40 \times 10^{13}$	3	$0.073 Ra^{0.245}$
26	3DFS	$6.40 \times 10^5 \leq Ra \leq 3.20 \times 10^8$	9	$0.308 Ra^{0.187}$
27	3DFS	$6.40 \times 10^{10} \leq Ra \leq 3.20 \times 10^{11}$	3	$0.358 Ra^{0.193}$

Table 4: Summary of least-squares fits to various scaling regimes. Where possible, we assess the sensitivity of the exponent by varying the range.

3.4. Discussion of the free-slip solutions

Turning to the 2DFS solutions, the most generous identification of the $p = 1/5$ regime in (3.5) is the five-decade range in row 20 of table 4. These 18 points correspond to the plateau $K_{1/5} = 0.25$ in figure 4(a). We are concerned, however, by 9 points in the first half of this range, i.e., row 21 of table 4. These 9 points undulate around the $K_{1/5} = 0.25$ plateau with an amplitude of about ± 0.01 and the least-squares exponent 0.186 is uncomfortably different from 1/5. These wayward points, at only moderately large Ra , correspond to solutions that are either steady, or weakly time dependent. Thus insufficient time-averaging in the estimate of Nu is not an issue. Moreover in this range the 2D and 3D solutions coincide. We conducted several tests by changing the spatial resolution and found no significant variation in the numerical estimate of Nu . If one views the exponent 0.186 as close to 1/5 then the wayward points are the lower end of a five-decade 2DFS scaling regime: the undulation is a pre-asymptotic imperfection in the first half of this regime. A more cautious interpretation is that the 2DFS $p = 1/5$ regime begins only at about $Ra = 6.40 \times 10^8$ and consists of the 9 points in row 22 of table 4. The 2DFS suite transitions to $p = 1/4$ scaling (3.6) at around $Ra = 10^{12}$ and forms the plateau at $K_{1/4} = 0.065$ in figure 4(b); see rows 23 through 25 of table 4.

The 3DFS solutions depart significantly from their 2DFS colleagues first at about $Ra = 3.20 \times 10^9$. There is no evidence of $p = 1/4$ scaling in the 3DFS suite. Instead, the three

3DFS solutions in row 27 of table 4 indicate a second $p = 1/5$ regime e.g. the 0.3 plateau in figure 4(a). We speculate that the **3DFS** suite is recapitulating the phenomenology seen in the **3DNS** suite: two $p = 1/5$ scaling regimes separated by a smooth transition. This speculation is based on the three solutions in row 27 which span less than one decade of variation in Ra .

4. Review of $Nu \sim Ra^{1/5}$ scaling arguments

Rossby (1965) proposed a visco-diffusive balance in the boundary layer adjacent to the non-uniformly heated surface and so arrived at the one-fifth scaling in (3.5). Rossby identified the length scale

$$\delta_{1/5} \stackrel{\text{def}}{=} Ra^{-1/5} h \quad (4.1)$$

as the thickness of the surface BL. In the following discussion we also need the length

$$\delta_{1/4} \stackrel{\text{def}}{=} Ra^{-1/4} h. \quad (4.2)$$

At $Ra = 6.4 \times 10^{13}$, the ratio of these two BL scales is $\delta_{1/5}/\delta_{1/4} \approx 5$.

Central to Rossby's $Pr \gg 1$ argument is the assumption that BL buoyancy forces are balanced by viscosity and that BL inertia is subdominant. At moderately large Ra , the exponent 1/5 has been supported by subsequent laboratory work and by numerical studies (Rossby 1998; Mularney *et al.* 2004; Siggers *et al.* 2004; Wang & Huang 2005; Chiu-Webster *et al.* 2008; Sheard & King 2011; Ilcak & Vallis 2012).

We emphasize that the $p = 1/5$ scaling (3.5), and the associated BL thickness $\delta_{1/5}$, seems not, however, to require that $Pr \gg 1$. The 2D solutions shown in figure 1 – including the unsteady solution in panels (c) and (d) – are well within the $K_{1/5} = 0.25$ regime of figure 4(a). Our unsteady **2DFS** solutions exhibit the one-fifth scaling (3.5) over at least three decades of Ra . All these $p = 1/5$ solutions have $Pr = 1$.

To further complicate the situation, 2D solutions in the $p = 1/4$ regime (3.6) still express the BL scale $\delta_{1/5}$. Figure 5 shows a progressively expanded view of the structure of HC near the upper surface. This **2DNS** solution is in the *non-Rossby* $p = 1/4$ scaling regime (3.6). Nonetheless, panel (d) of figure 5 indicates that $\delta_{1/5}$ is a useful BL length scale. We conclude that at sufficiently high Ra there is a double BL: a thin- $\delta_{1/4}$ layer is nested within a thicker $\delta_{1/5}$ -layer. We discuss this double BL further in section 5.

(The **2DNS** solution in figure 5(a) exhibits the vortex-gas phenomenology noted previously in the **2DFS** solutions shown in figure 2. At high Ra , no matter the viscous boundary condition, the interior of 2D HC is characterized as a vortex gas.)

As an alternative to Rossby scaling, Shishkina *et al.* (2016) proposed a set of scaling arguments summarized in a phase diagram of the (Ra, Pr) -plane. This diagram shows high- Pr regions denoted I_ℓ^* , I_∞ and III_∞ ; these three high- Pr regions have $Nu \sim Ra^p$ with $p = 1/4$ in I_ℓ^* and III_∞ and $p = 1/6$ in I_∞ . This tripartite proposal cannot be reconciled with the $Pr \gg 1$ results of Rossby (1965), Chiu-Webster *et al.* (2008) and Ramme & Hansen (2019). In the phase diagram of Shishkina *et al.* (2016), the $p = 1/5$ scaling is found only in the $Pr \ll 1$ region I_ℓ . We discuss region I_ℓ in more detail below.

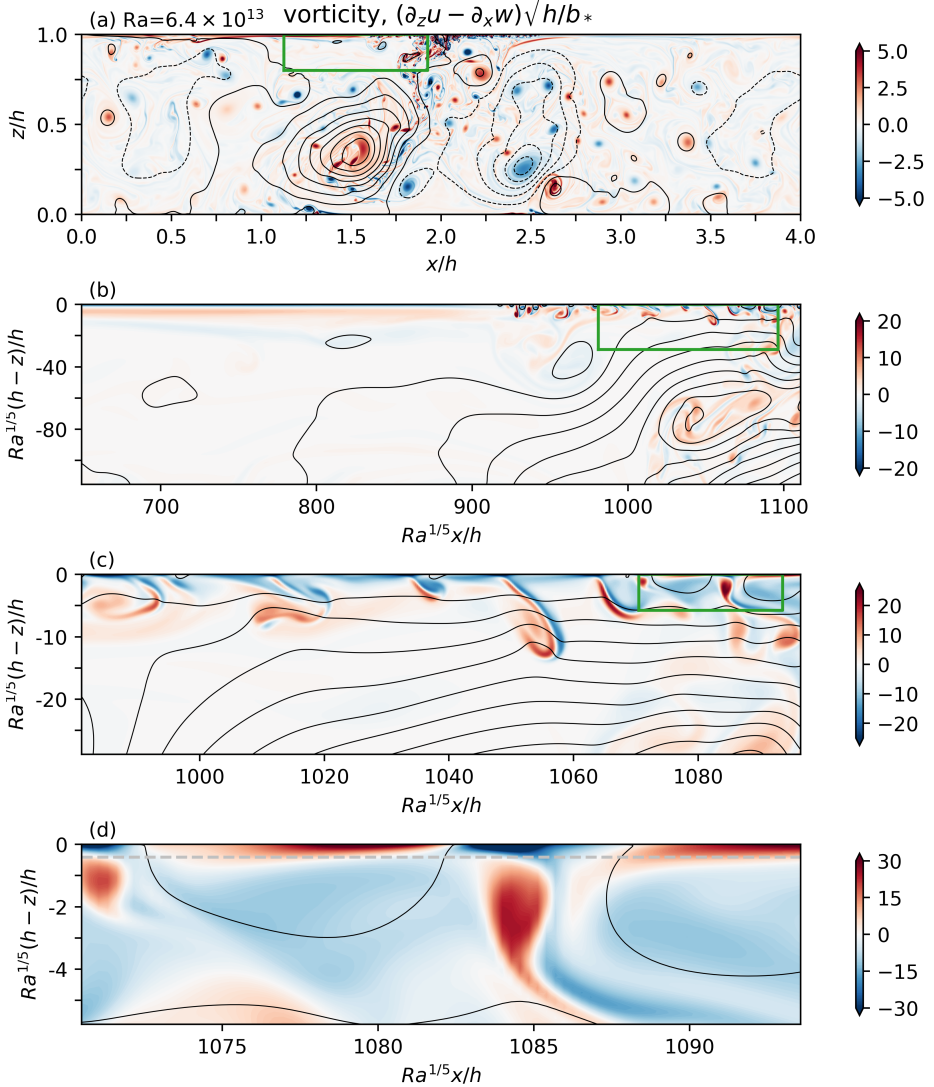


Figure 5: (a) A snapshot of vorticity in the 2DNS solution at $Ra = 6.4 \times 10^{13}$; this solution is in the non-Rossby $Nu \sim Ra^{1/4}$ scaling regime. Panels (b)-(d) depict the boundary-layer structure by progressively zooming in to the top surface. Green rectangles in panels (a), (b) and (c) indicate the regions in panels (b), (c) and (d) respectively. In panels (b), (c) and (d), both axes are measured in units of $\delta_{1/5}$. The dashed grey line in panel (d) indicates the distance $2\delta_{1/4}$ below the top surface $z = h$. The contours in all panels are streamlines.

4.1. The spanwise average

To identify the various processes in the BL, we begin taking a spanwise y -average of the equations of motion. Denote this spanwise average with a hat so that

$$b(x, y, z, t) = \underbrace{\frac{1}{\ell_y} \int_0^{\ell_y} b(x, y, z, t) \, dy}_{\stackrel{\text{def}}{=} \hat{b}(x, z, t)} + b'(x, y, z, t). \quad (4.3)$$

Above, $b'(x, y, z, t)$ is the three-dimensional departure from the spanwise average. Taking the spanwise average of the 3D continuity equation (2.3), we obtain a 2D “overturning stream function” $\psi(x, z, t)$, such that $(\hat{u}, \hat{w}) = (-\psi_z, \psi_x)$. With this notation the 3D velocity is written as

$$(u, v, w) = (-\psi_z, 0, \psi_x) + (u', v', w') . \quad (4.4)$$

The spanwise-average of the buoyancy equation is

$$\hat{b}_t + \psi_x \hat{b}_z - \psi_z \hat{b}_x + \partial_x \widehat{u' b'} + \partial_z \widehat{w' b'} = \kappa \nabla^2 \hat{b} , \quad (4.5)$$

and the spanwise average of the spanwise vorticity equation is

$$\underbrace{\zeta_t + \psi_x \zeta_z - \psi_z \zeta_x}_{\text{inertia}} + \underbrace{\hat{b}_x}_{\text{buoyancy torque}} + \underbrace{(\partial_z^2 - \partial_x^2) \widehat{u' w'} + \partial_x \partial_z (\widehat{u'^2} - \widehat{w'^2})}_{\text{Reynolds stress torque (RST)}} = \underbrace{\nu \nabla^2 \zeta}_{\text{viscosity}} . \quad (4.6)$$

Above $\zeta \stackrel{\text{def}}{=} -\nabla^2 \psi$ is the spanwise-averaged spanwise vorticity. The power integral (2.8) becomes

$$\varepsilon = \nu \langle \zeta^2 \rangle + \nu \langle |\nabla \mathbf{u}'|^2 \rangle \quad (4.7)$$

$$= -\kappa \bar{b}(0)/h . \quad (4.8)$$

The 2D equations of motion are recovered by suppressing the spanwise averages of quadratic fluctuations in (4.5), (4.6), and (4.7) e.g. the 2D vorticity equation is (4.6) without RST.

4.2. A review of $Nu \sim Ra^{1/5}$ scaling arguments

Following Shishkina *et al.* (2016), we assume that there is a BL with thickness δ_b in buoyancy and δ_u in momentum and vorticity. The Reynolds number is

$$Re \stackrel{\text{def}}{=} \frac{U h}{\nu} , \quad (4.9)$$

where

$$U \stackrel{\text{def}}{=} \sqrt{\langle |\mathbf{u}|^2 \rangle} \quad (4.10)$$

is the typical flow velocity. The domain length scales ℓ_x , ℓ_y and h are roughly comparable. We use the depth h as representative of the domain length scale.

Scale analysis of the surface Nusselt number in (2.11), e.g., $\hat{b}_z(h) \sim b_\star/\delta_b$, shows that

$$Nu \sim \frac{h}{\delta_b} . \quad (4.11)$$

One reaches the same conclusion via scale analysis of the χ -based Nusselt number in (2.9): although $|\nabla b|^2 \sim b_\star^2/\delta_b^2$, the χ -BL occupies only a fraction δ_b/h of the domain. Thus (4.11) follows because of the volume average $\langle \cdot \rangle$.

Now apply scale analysis to the buoyancy equation (4.5). Using results such as $\psi_z \hat{b}_x \sim \psi_x \hat{b}_z \sim U b_\star/h$ and $\kappa \nabla^2 \hat{b} \sim \kappa b_\star/\delta_b^2$ one has

$$U \sim \frac{\kappa h}{\delta_b^2} , \quad \text{or in non-dimensional form} \quad Nu \sim (Re Pr)^{1/2} . \quad (4.12)$$

To estimate the viscous dissipation ε on the right of the power integral (4.7), one assumes that an order-one fraction of ε is concentrated in the BL, and this BL occupies a fraction δ_u/h of the domain. One can either neglect $\nu \langle |\nabla \mathbf{u}'|^2 \rangle$, or assume that both terms on the right

of (4.7) scale in the same way, i.e., as $\nu\zeta^2 \sim \nu(U/\delta_u)^2$. In either case

$$\varepsilon \sim \frac{\nu U^2}{\delta_u h}. \quad (4.13)$$

Scale analysis of the right hand side of (4.8) assumes that the bottom buoyancy, $\bar{b}(0)$, is an order-one fraction of the minimum buoyancy, $-b_\star$, on the top surface. (The stronger result that $\bar{b}(0) \rightarrow -b_\star$ as $Ra \rightarrow \infty$ is likely true.) Thus

$$\varepsilon \sim \frac{\kappa b_\star}{h}. \quad (4.14)$$

Combining (4.13) and (4.14)

$$U^2 \sim \frac{\kappa}{\nu} \delta_u b_\star, \quad \text{or in non-dimensional form} \quad (RePr)^2 \sim \frac{\delta_u}{h} Ra. \quad (4.15)$$

Eliminating $RePr$ between (4.12) and (4.15), and then using (4.11) to get rid of h , one finds

$$Nu^5 \sim \frac{\delta_u}{\delta_b} Ra. \quad (4.16)$$

The final step to obtain the dependence of Nu on Ra and Pr is to express the ratio δ_u/δ_b on the right of (4.16) in terms Ra and Pr . There are three arguments in the literature.

The scaling of Rossby (1965). Taking $\delta_u = \delta_b$ one obtains from (4.16)

$$Nu \sim Pr^0 Ra^{1/5} \quad \text{and} \quad Re \sim Pr^{-1} Ra^{2/5}. \quad (4.17)$$

Rossby's 1965 argument did not employ the power integral and its consequence (4.16). Instead, Rossby assumes *ab initio* that $\delta_b = \delta_u$ and balances buoyancy torque with viscosity in (4.6), leading to $U \sim b_\star \delta_u^3 / \ell \nu$. Combining these results with (4.11) and (4.12) one again finds (4.17). Rossby's balance between buoyancy torque and viscosity applies to both **FS** and **NS**. In the **FS** case, the velocity BL results from the vorticity source \hat{b}_x in (4.6): this rationalization of Rossby's assumption that $\delta_u = \delta_b$ also applies to **NS**.

The scaling of Gayen, Griffith & Hughes (2014). In the vorticity equation (4.6), balance buoyancy torque with either inertia or Reynolds stress torques, leading to $U^2 \sim \delta_u b_\star$, and follow Rossby by assuming that $\delta_b = \delta_u$. Combining these results with (4.11) and (4.12) one finds

$$Nu \sim Pr^{1/5} Ra^{1/5} \quad \text{and} \quad Re \sim Pr^{-3/5} Ra^{2/5}. \quad (4.18)$$

This argument does not use the power integral and it is not consistent with (4.16) unless Pr is order unity. Using the scaling assumptions above to estimate ε in (4.7) and (4.8) we find

$$\nu \langle \zeta^2 \rangle \sim Ra (\kappa \nu^2 / h^4) \quad \text{and} \quad -\kappa \bar{b}(0)/h \sim Ra (\kappa^2 \nu / h^4). \quad (4.19)$$

The two terms in (4.19) differ by a factor of Pr : this is a problem if Pr is either very large or very small. But with Pr of order unity – and here we consider $Pr = 1$ – there is no problem closing the mechanical energy budget and thus the scaling of **Gayen et al. (2014)** is a valid alternative to that of Rossby.

The scaling of Shishkina, Grossman & Lohse (2016). In the vorticity equation (4.6), balance inertia with viscosity, leading to $U \sim \nu h / \delta_u^2$. Eliminating U with (4.12) one finds $\delta_u = Pr^{1/2} \delta_b$, and substituting into the power-integral (4.16)

$$Nu \sim Pr^{1/10} Ra^{1/5}, \quad \text{and} \quad Re \sim Pr^{-4/5} Ra^{2/5}. \quad (4.20)$$

A distinctive feature of this scaling argument is that buoyancy torque \hat{b}_x in (4.6) does not appear in the leading-order BL vorticity balance. This is justified by requiring that $Pr \ll 1$, so

that $\delta_u = Pr^{1/2} \delta_b \ll \delta_b$. In other words, this visco-inertial BL is so thin that both viscosity and inertia are much greater than the buoyancy torque $\hat{b}_x \sim b_\star/h$.

Despite different physical assumptions, the three arguments summarized above are in agreement that $Nu \sim Ra^{1/5}$. All differences lie in the predicted dependence of Nu on Pr . Moreover the three groups have presented numerical evidence in support of their particular Pr -exponent (Rossby 1998; Gayen *et al.* 2014; Shishkina & Wagner 2016). Perhaps the different surface buoyancy profiles used by the three groups is important? It is beyond our scope here to contribute further to investigation of the Pr -exponent and the possible influence of the surface buoyancy profile.

We close this review by noting that the nomenclature used to designate scaling (4.20) – corresponding to region I_ℓ in the phase diagram of Shishkina *et al.* (2016) – needs clarification. Region I_ℓ , with $Pr \ll 1$, is referred to by Shishkina *et al.* (2016) as “Rossby scaling”. Although $p = 1/5$ is the same as Rossby, the dependence on Pr in (4.20) differs from that of Rossby in (4.17). Moreover Rossby was concerned with $Pr \gg 1$, while scaling (4.20) ostensibly applies with $Pr \ll 1$. Referring to I_ℓ as Rossby scaling is a misnomer: the phase diagram of Shishkina *et al.* (2016) does not contain a region corresponding to the original $Pr \gg 1$ Rossby scaling in (4.17).

4.3. BL balance of terms in the vorticity equation (4.6)

All solutions in this work have $Pr = 1$ and we have nothing to say regarding the different Pr -exponents in (4.17), (4.18), and (4.20). We can, however, examine the balance of terms in the spanwise-averaged vorticity equation (4.6) and so assess the assumptions made by the three scaling arguments summarized above. To compactly present these results we further x -average (4.6) over the interval $0 < x/h < 1.85$ at fixed z . By stopping the x -average at $x/h = 1.85$, we stay away from the moving attachment point of the plume. (Recall that the midpoint of the domain, which is also the position of maximum surface density, is at $x = 2h$.) The x -average of (4.6) also removes small-scale fluctuations that dominate the BL at the highest values of Ra , e.g. see figure 5(c) and (d). There is no time averaging: this partial x -average is applied to a single snapshot.

In the following discussion we nominally define the main boundary layer (MBL hereafter) as the region within $2\delta_{1/5}$ from the top surface:

$$h - 2\delta_{1/5} \leq z \leq h, \quad (4.21)$$

and the inner boundary layer (IBL hereafter) as the region within $2\delta_{1/4}$ from the top surface:

$$h - 2\delta_{1/4} \leq z \leq h. \quad (4.22)$$

4.3.1. The 2D solutions

Figure 6 shows the balance of terms in the 2D version of (4.6). There is no Reynolds stress torque (RST) in 2D.

The MBL in figure 6(a) and (b) is exemplary of the two-term Rossby balance between buoyancy torque and viscosity. In fact the 2DFS solutions in the top row of figure 6 are characterized very simply: inertia is subdominant in the 2DFS MBL. This even applies to the $Ra = 6.4 \times 10^{13}$ solution in figure 6(c), which is in the $p = 1/4$ regime with $K_{1/4} = 0.065$ in figure 4(b). Below the MBL the situation is more complicated: in figure 6(c), there is cancellation between viscosity and inertia. In this region, below the MBL, buoyancy torque is not negligible: there is a three-term balance between buoyancy torque, viscosity and inertial in the 2DFS vorticity equation. The 2DFS solutions are remarkable because Rossby’s balance applies throughout the MBL up to the maximum $Ra = 6.4 \times 10^{13}$ i.e. Rossby’s balance applies even in the $p = 1/4$ non-Rossby scaling regime.

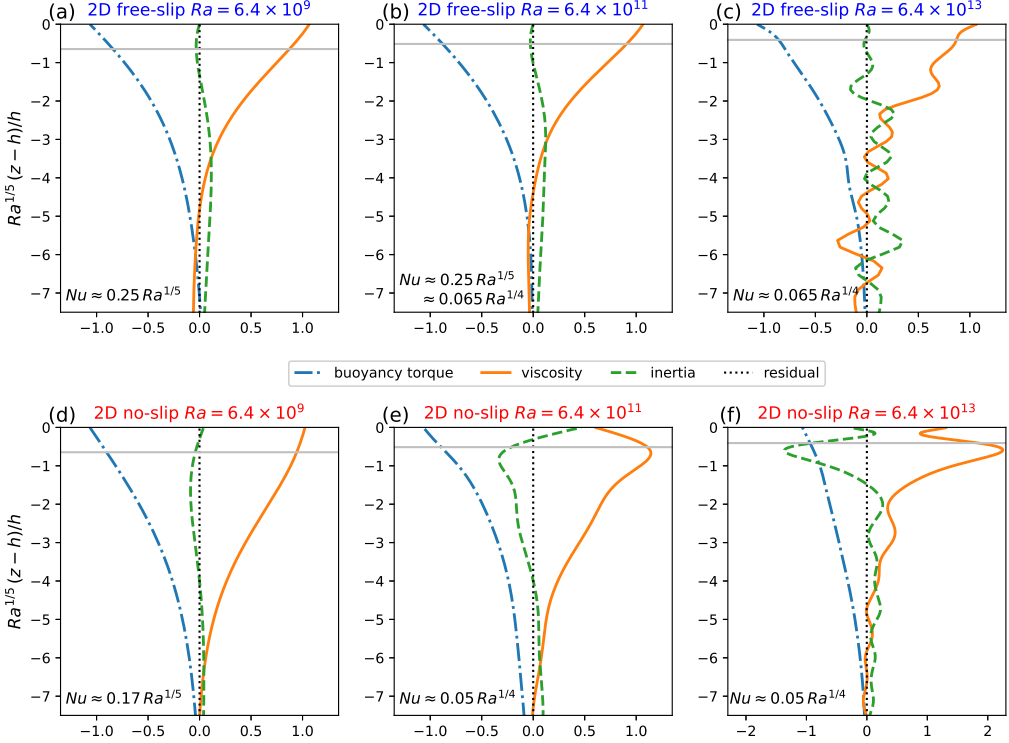


Figure 6: Three terms in the 2D version of the vorticity equation (4.6). The top row shows 2DFS solutions and bottom row shows 2DNS solutions. The abscissa scale is expanded in (f). Solutions above are in the scaling regimes indicated in the bottom left corner of each panel; the solution in (b) is at a transition between one-fifth and one-fourth. All terms are non-dimensionalized using b_\star/h , e.g. buoyancy torque is $b_x h/b_\star$. Horizontal grey lines indicate the distance $2\delta_{1/4}$ below the top surface $z = h$.

For the 2DNS solutions in the bottom row of figure 6, the situation is more complicated. The base of the IBL in (4.22) is indicated by the grey horizontal lines in figure 6. It is striking that in figure 6(e) and (f), inertia is largest within the IBL and that there is a three-term balance in the 2DNS vorticity equation.

Examination of the vorticity equation (4.6) evaluated at the surface $z = h$ provides a rationalization for the different role of inertia in 2DFS versus 2DNS. At $z = h$ the inertia term in (4.6) is

$$\text{inertia} \stackrel{\text{def}}{=} \zeta_t + \psi_x \zeta_z - \psi_z \zeta_x, \quad (4.23)$$

$$= \begin{cases} 0, & \text{with FS boundary conditions } (\zeta = 0); \\ \zeta_t, & \text{with NS boundary conditions } (\psi_x = \psi_z = 0). \end{cases} \quad (4.24)$$

In the 2DFS case inertia is identically zero at the surface and there must therefore be a balance between the two remaining terms in the 2D version of (4.6), i.e. at $z = h$ viscosity must balance buoyancy torque. In fact this Rossby balance applies throughout the 2DFS MBL.

In the 2DNS case, inertia in (4.6) might be non-zero if there are temporal fluctuations so that $\zeta_t \neq 0$. In figure 6(d) these ζ_t fluctuations are small, and so is inertia. As the Ra is increased, e.g. in figure 6(e) and (f), the temporal fluctuations are larger and inertia at the surface $z = h$ becomes comparable to buoyancy torque and viscosity.

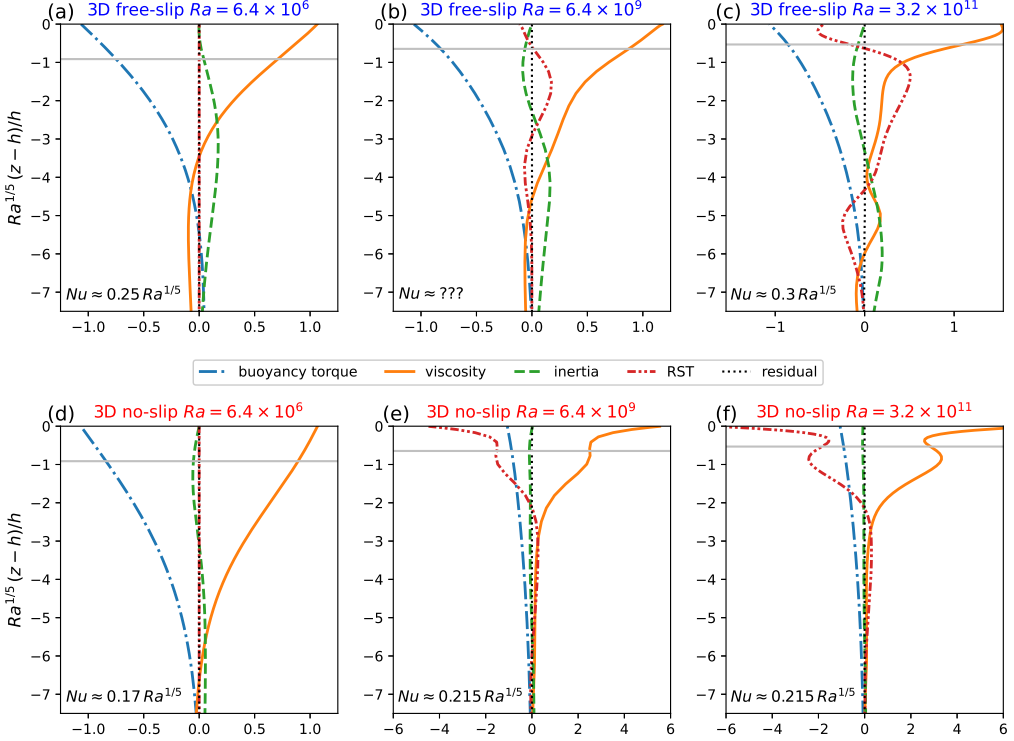


Figure 7: Four terms in the vorticity equation (4.6), averaged over $0 \leq x/h \leq 1.85$, and calculated from snapshots of the 3D solutions. The top row shows 3DFS solutions and bottom row shows 3DNS solutions. The abscissa scale varies between the panels. Solutions above are in the scaling regimes indicated in the bottom left corner of each panel. In panel (b) $Nu = ???$ indicates that this solution is in the transition between the two $p = 1/5$ regimes in (a) and (c). All terms are non-dimensionalized using b_\star/h , e.g. buoyancy torque is $b_x h/b_\star$. Horizontal grey lines indicate the distance $2\delta_{1/4}$ below the surface.

The argument above requires qualification in the special – but popular – case of piecewise constant $b_s(x)$, e.g. $b_s(x) = \pm b_\star$, with a discontinuous jump at the middle of the domain. While (4.24) is valid, the buoyancy torque \hat{b}_x at the surface vanishes, except at the discontinuity. In this case the 2D version of (4.6) everywhere except the discontinuity, when evaluated at the wall, collapses to $\zeta_t = v\nabla^2\zeta$ and no conclusion can be drawn. This observation is perhaps an indication that piecewise constant buoyancy profiles might be qualitatively different from smoothly varying buoyancy profiles.

4.3.2. The 3D solutions

In figure 7 we turn to the 3D solutions and analyze the balance of terms in the spanwise-averaged vorticity equation (4.6). In 3D the term RST in (4.6) might be non-zero.

We use the partial x -average described in the previous section. From the outset we draw attention to a simple result: within the MBL of figure 7, inertia in the 3D vorticity equation (4.6) is always subdominant relative to the other three terms. The unimportance of MBL inertia is striking in the NS solutions in bottom row of figure 7 – but it is also a not-bad approximation for the FS solutions in the top row.

The 3DFS solution in figure 7(a) is at the low Rayleigh number 6.4×10^6 and is effectively 2D and steady. This solution, which is in the middle of a four-decade $p = 1/5$ regime with

$K_{1/5} = 0.25$, exhibits a two-term Rossby balance between viscosity and buoyancy torque. Inertia becomes as large as viscosity just below the MBL.

Figure 7(d) shows a **NS** solution from the middle of the first $p = 1/5$ scaling regime – with $K_{1/5} = 0.17$ in figure 4(a). Figures 7(e,f) show solutions from the second $p = 1/5$ scaling regime with $K_{1/5} = 0.215$. In figure 7(d) there is a Rossby balance between viscosity and buoyancy torque, while in figures 7(e,f) the situation is complicated: close to the top surface, within the IBL, there is a two-term balance between RST and viscosity. Further from the surface, but within the MBL, there is a three-term balance involving viscosity, buoyancy torque and RST.

The **3DNS** solutions in the bottom row of figures 7 confirm the result of [Gayen et al. \(2014\)](#): the difference between the two **3DNS** $p = 1/5$ regimes results from a transition between a low- Ra Rossby balance in panel (a) to an unsteady 3D BL flow involving large RST in panels (e) and (f).

4.3.3. Summary and conclusion based on the BL balance of terms

The twelve panels in figures 6 and 7 summarize results from twelve solutions, with both **FS** and **NS** boundary conditions, and both 2D and 3D configurations. The main conclusions are:

- (i) the structure of the buoyancy torque is the same in the twelve cases;
- (ii) in the $p = 1/5$ and $p = 1/4$ regimes the thickness of the buoyancy-torque BL is $\delta_{1/5}$;
- (iii) buoyancy torque is of leading importance in ten of the twelve cases, and in seven cases Rossby's two-term balance between buoyancy torque and viscosity holds throughout the MBL;
- (iv) the buoyancy torque is subdominant only for the **3DNS** solutions at the highest Ra 's, resulting in a two-term balance between viscosity and RST;
- (v) in the high- Ra **NS** solutions, there is a thin $\delta_{1/4}$ -IBL nested within the thicker $\delta_{1/5}$ -MBL.

Points (i) and (ii) indicate that main features of the buoyancy field are insensitive to the balance of terms in the vorticity equation, and to the viscous boundary condition and to dimensionality. Point (iii) indicates that Rossby's $Pr \gg 1$ balance of terms can apply at moderately large Ra even with $Pr = 1$.

All solutions exhibit the same $Nu-Ra$ scaling phenomenology, even though the balance of terms in the vorticity equation changes with viscous boundary condition and dimensionality. For example, in the 2D results in figure 6, inertia plays a different role in the top row (**FS**) than in the bottom row (**NS**). Yet the transition from $p = 1/5$ to $p = 1/4$ is qualitatively the same for the two viscous boundary conditions.

5. Nested boundary layers

[Tsai et al. \(2020\)](#) investigate **2DNS** HC with $Pr = 6.14$. With $Ra > 10^{10}$, and provided that the imposed surface buoyancy varies linearly with the horizontal coordinate x , [Tsai et al. \(2020\)](#) report the $p = 1/4$ scaling (3.6) extending over four decades of Ra . Here we also find $p = 1/4$ in the **2DFS** and **2DNS** solution suites. [Tsai et al. \(2020\)](#) speculate that the $p = 1/4$ scaling might correspond to a regime proposed by [Shishkina et al. \(2016\)](#) in their phase diagram of the (Ra, Pr) parameter plane. In this scheme the (Ra, Pr) -plane is partitioned into seven regions and the exponent $1/4$ is located in regions denoted III_∞ , IV_u , and I_ℓ^* . But we now show that defining features of III_∞ , IV_u , and I_ℓ^* do not agree with the numerical solutions. We conclude that $p = 1/4$ found here, and likely also in [Tsai et al. \(2020\)](#), is not in agreement with any region of the phase diagram of [Shishkina et al. \(2016\)](#).

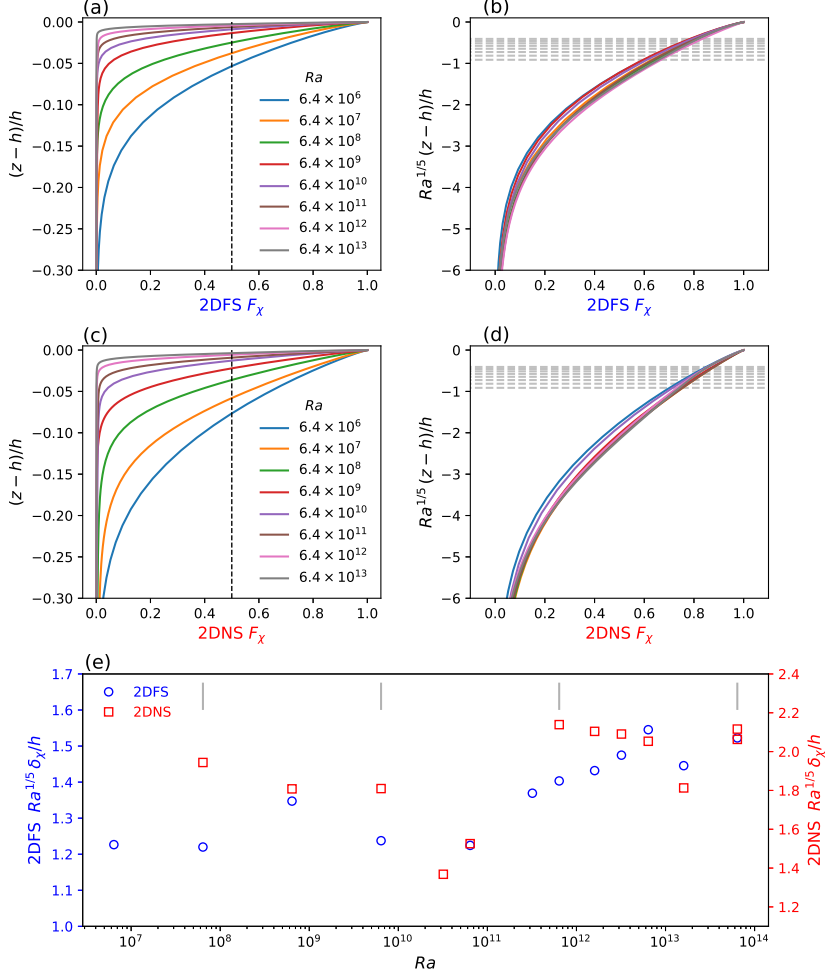


Figure 8: (a) The function $F_\chi(z)$ defined in (5.1) for the 2DFS solutions. A BL thickness, δ_χ , is defined as the distance from the top at which $F_\chi(z) = 1/2$ (dashed vertical lines in panel (a)). (b) Same as (a) but with the vertical axis rescaled with $Ra^{1/5}$. Horizontal grey dashed lines indicate the distance $2\delta_{1/4}$ below the top surface $z = h$. Panels (c) and (d) are the same as (a) and (b) respectively but for the 2DNS solutions. (e) The compensated BL thickness, $Ra^{1/5}\delta_\chi/h$, as a function of Ra for both the 2DFS and the 2DNS solutions. The four vertical grey line segments mark the Ra 's of the solutions in figures 1 and 2.

5.1. Partitioning of buoyancy dissipation χ between BL and interior

A main characteristic distinguishing the various regimes by Shishkina *et al.* (2016) is the partitioning of kinetic energy dissipation, ε , and buoyancy variance dissipation, χ , between the BL and the interior of the domain. To quantify the partitioning of χ we introduce the function

$$F_\chi(z) \stackrel{\text{def}}{=} \frac{\kappa}{h\chi} \int_0^z \overline{|\nabla b|^2} dz', \quad (5.1)$$

where the overbar denotes an (x, y, t) -average. $F_\chi(z)$ in figure 8 increases monotonically from 0 to 1 with z/h and indicates the fraction of buoyancy-variance dissipation below the level z . Figures 8(a) and (c) show that χ is increasingly localized within a BL as $Ra \rightarrow \infty$.

A main characteristic of regions III_∞ and IV_u in the phase diagram of Shishkina *et al.* (2016) is that χ is dominant in the interior of the domain. Thus figures 8(a) and (c) disqualify regions III_∞ and IV_u . The remaining possibility with exponent $1/4$ is the $Pr \gg 1$ region I_ℓ^* , characterized by a momentum BL that is much thicker than the buoyancy diffusion BL. But region I_ℓ^* is located at moderate values of Ra in the phase diagram so that $1/4$ is the first exponent encountered if Pr is fixed and Ra is increased from small values. In our 2D solutions, however, we first find $p = 1/5$ scaling (3.5), which is replaced at higher Ra by $p = 1/4$ in (3.6). This is also the case in the study of Tsai *et al.* (2020): first $1/5$ and then, at higher Ra , $1/4$. We conclude that $p = 1/4$ in the 2D solution suites is not related to regions III_∞ , IV_u and I_ℓ^* of the phase diagram of Shishkina *et al.* (2016). In section 6 we seek an alternative explanation for the $p = 1/4$ regimes in figure 4(b).

To extract more information from $F_\chi(z)$, we scale the z -axis with $\delta_{1/5}$ and re-plot the results from figures 8(b) and (d). The curves now fall largely on top of each other, indicating that the function $F_\chi(z)$ expresses the BL thickness $\delta_{1/5}$, even if $Nu \sim Ra^{1/4}$. To quantify this, we define a BL thickness, δ_χ , by determining the level at which $F_\chi(z) = 1/2$: see the dashed vertical line in figures 8(a) and (c). The compensated plot in figure 8(e) then shows that

$$\delta_\chi \approx K_\chi \delta_{1/5}. \quad (5.2)$$

The constant K_χ in (5.2) is about 1.5 for the FS solutions and 1.8 for the NS solutions.

The scaling in (5.2) applies in *both* the $p = 1/5$ regime (3.5) and the $p = 1/4$ regime (3.6). Yet the reasoning in section 4, leading to

$$Nu \sim \frac{h}{\delta_b}, \quad (5.3)$$

underpins all scaling arguments and seems inescapable. It must be that in the $p = 1/4$ regime (3.6), the buoyancy BL has a double-layer structure: there is a thin BL, with thickness $\delta_b = \delta_{1/4}$, embedded within the thicker δ_χ -BL in (5.2). In the next section we show the existence of such a double BL.

(The scatter of K_χ in figure 8(c) might be considered uncomfortably large. Note, however, that Ra is varied by seven decades. This large range encompasses the transition from steady to strongly time-dependent 2D flows. At $Ra = 6.4 \times 10^{13}$, $Ra^{-1/4}$ is smaller than $Ra^{-1/5}$ by a factor of 5, which is much greater than the $\pm 20\%$ scatter in figure 8(c).)

5.2. The $\delta_{1/4}$ -boundary layer

To identify the $\delta_{1/4}$ -BL in our solutions, and show consistency with (5.3) in the $p = 1/4$ regime, we notice that with the sinusoidal surface buoyancy in (2.4), the surface Nusselt number (2.11) is

$$Nu_s = b'_1(h) / b'_{\text{diff}}(h), \quad (5.4)$$

where above the prime denotes a z -derivative and

$$b_1(z) \stackrel{\text{def}}{=} 2 \overline{\cos kx b(x, y, z, t)}. \quad (5.5)$$

Using (5.4) we obtain an alternative expression for δ_b :

$$\delta_b \stackrel{\text{def}}{=} b_\star / b'_1(h), \quad (5.6)$$

where b_\star is the amplitude of the sinusoidal surface buoyancy in (2.4). The numerator in (5.6) is appropriate because $b_\star = b_1(h) = b_{\text{diff}}(h)$.

Figure 9 shows $b_1(z)$, and the first two derivatives of $b_1(z)$. The overline in (5.5) indicates

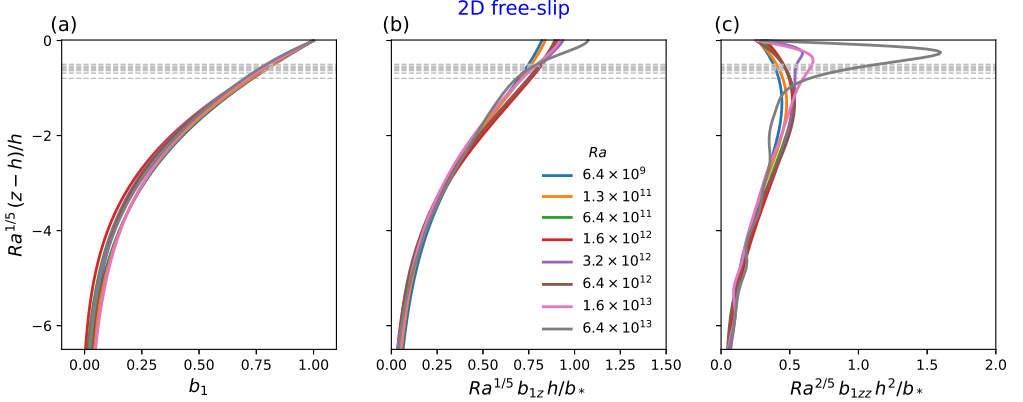


Figure 9: The structures of (a) $b_1(z)$, (b) $b'_1(z)$, and (c) $b''_1(z)$ for 2DFS solutions at various Ra . $b_1(z)$ was obtained here from the final snapshot without any time-averaging. Horizontal grey dashed lines indicate the distance $2\delta_{1/4}$ below the top surface $z = h$.

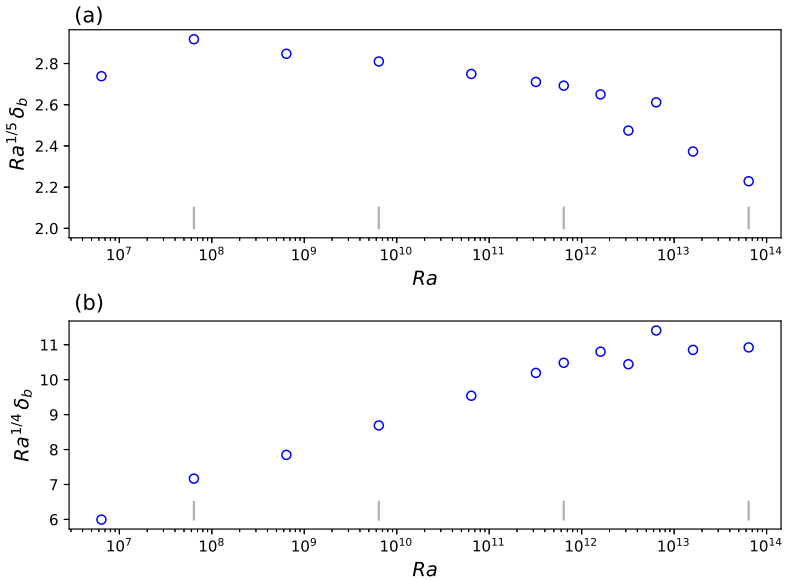


Figure 10: The compensated surface BL thickness, δ_b in (5.6), for the 2DFS suite. In panel (a) δ_b is compensated by $Ra^{-1/5}$ and in (b) by $Ra^{-1/4}$. The transition between the $p = 1/5$ scaling (3.5) and the $p = 1/4$ scaling (3.6) is at about $Ra = 10^{12}$. Vertical grey line segments mark the Ra values corresponding to the solutions in figures 1 and 2.

both a horizontal and temporal average. Figure 9 is based on the horizontal average of single snapshots of the buoyancy field at the final time. The inner BL, with thickness $\delta_{1/4}$, is not visible in $b_1(z)$ in figure 9(a). But the higher derivatives of $b_1(z)$ in the panels (b) and (c) reveal the scale $\delta_{1/4}$. In particular, the $p = 1/4$ scaling (3.6) results from the increase in $b'_1(h)$, evident in figure 9(b) as Ra increases. The maximum of $b''_1(z)$ in figure 9(c) appears only in the $p = 1/4$ regime (3.6).

Figure 10(a) shows δ_b , diagnosed from (5.6), and compensated by $Ra^{1/5}$. For Ra 's corresponding to $p = 1/5$ scaling this compensated δ_b in the narrow range 2.6 and 2.9. Thus with $p = 1/5$, both δ_b and δ_χ vary as $\delta_{1/5}$. Figure 10(b) shows that at the four or five highest values of Ra , corresponding to the $p = 1/4$ scaling, δ_b compensated with $Ra^{1/4}$ varies between about 10.5 and 11.4. We conclude that in the $p = 1/4$ regime $\delta_b \sim \delta_{1/4}$, but $\delta_\chi \sim \delta_{1/5}$.

6. A scaling argument for $Nu \sim Ra^{1/4}$

In this section we present a scaling argument applicable to the $p = 1/4$ regime of horizontal convection. Although our numerical solutions revealed the $p = 1/4$ scaling only in the 2D cases, we still hold hope that $p = 1/4$ might also emerge in 3D at sufficiently high Ra . With the 3D case in mind, we propose an overarching explanation for the $p = 1/4$ scaling – independent of boundary conditions, dimensionality and 2D vortex-gas phenomenology.

The $p = 1/4$ regime requires an inner buoyancy BL with thickness $\delta_b \sim \delta_{1/4}$. In discussing this inner BL it is helpful to keep figure 5(d) in mind: the $\delta_{1/4}$ -BL is identified by the dashed grey line. Think of this inner BL as a laminar sub-layer, stirred by the outer flow in the much thicker $\delta_{1/5}$ -BL. The overarching explanation alluded to above is that the thickness of the laminar sub-layer is related to the Kolmogorov and Batchelor length scales

$$\eta_K = \left(\frac{\nu^3}{\varepsilon} \right)^{1/4} \quad \text{and} \quad \eta_B = \left(\frac{\kappa^2 \nu}{\varepsilon} \right)^{1/4}. \quad (6.1)$$

These length scales are identified as the smallest scales of fluctuations in momentum and buoyancy that can survive before the damping by viscosity ν and diffusion κ is overwhelming. By analogy, the HC laminar sub-layer with thickness δ_b is the thinnest BL that can survive in a horizontal-convective flow that is supplied with kinetic energy at a rate ε .

(In the arguments of Kolmogorov and Batchelor the viscous dissipation rate ε is also the energy cascade rate in a 3D inertial range. This interpretation of ε cannot apply to 2D HC: there is no vortex stretching in a 2D flow and therefore no forward cascade of energy. We argue instead that the laminar sub-layer thickness is determined by ε as the most basic measure of forcing strength and by the molecular parameters ν and κ . Thus $\delta_b \sim (\nu^p \kappa^q / \varepsilon)^{1/4}$, with $p + q = 3$, is dimensionally acceptable; η_K and η_B are the most prominent members of this family. Saying more would require varying Pr which is beyond our scope here.)

Following the scaling arguments reviewed section 4, we assume that $\bar{b}(0) \approx -b_\star$. Then, once again, the energy power integral (2.8) implies that

$$\varepsilon \sim \frac{\kappa b_\star}{h}. \quad (6.2)$$

With ε in (6.2), η_K and η_B in (6.1) can be written as

$$\frac{\eta_K}{h} = Pr^{1/2} Ra^{-1/4} \quad \text{and} \quad \frac{\eta_B}{h} = Pr^0 Ra^{-1/4}. \quad (6.3)$$

Thus if the laminar sub-layer has thickness $\delta_b \sim \eta_K$, or perhaps $\delta_b \sim \eta_B$, then from (4.11) $Nu \sim Ra^{1/4}$.

7. Dimensionality and mean square vorticity

With periodicity in the spanwise direction, 2D solutions are also 3D solutions. At sufficiently high Ra , and with sufficiently large ℓ_y , these 2D solutions are unstable to perturbations in the spanwise dimension (Gayen *et al.* 2014; Tsai *et al.* 2016; Passaggia *et al.* 2017). Apart from

the possibility of non-zero RST in (4.6) the scaling arguments summarized in section 4 make no reference to the development of 3D flow. To appreciate the limitations of scaling arguments it is interesting to compare 2D and 3D solutions at the same Ra . Comparison of 3D with 2D is also relevant to the nature of turbulence in HC (Paparella & Young 2002; Scotti & White 2011; Shishkina *et al.* 2016), e.g., turbulent amplification of vorticity by vortex stretching does not operate in 2D.

Once 3D motion is activated by instabilities one expects initiation of vortex stretching and the development of other associated qualitative differences between 2D and 3D HC. But this cannot happen in HC: in this section we show using the mechanical energy power integral (2.8) that in the limit $Ra \rightarrow \infty$ vorticity amplification does not occur in the 3D HC. To motivate this proof we first note the rather small quantitative differences between 2D and 3D HC at $Ra = 3.2 \times 10^{11}$.

In table 1 it is remarkable that the 3D solutions have less than a 20% enhancement of Nu above that of the 2D solutions at the same Ra . It is difficult to believe that this modest 20% enhancement extends to geophysical Ra 's, which exceed the largest 3D Ra 's in table 1 by perhaps 10^{12} . If the 3D increase in Nu remains at 20%, then relatively inexpensive 2D numerical solutions would provide useful estimates of 3D heat transport.

(It is likely that the 2D Nu is always less than the 3D Nu i.e. the onset of 3D motion cannot be accompanied by a decrease in heat transport. A proof of this conjecture would be useful.)

To further emphasize the small 3D increase in Nu , notice that boundary conditions have a larger quantitative effect on heat transport than dimensionality: in figure 4 the **2DFS** solutions have larger Nu than the **3DNS** solutions.

Table 5 summarizes gross measures of the departures from the 2D spanwise-averaged circulation defined in (4.3). For both both our highest- Ra **3DNS** and **3DFS** solutions, about two-thirds of the kinetic energy is in the spanwise-averaged flow. In the third column the component of buoyancy gradient in the spanwise direction (b_y) contributes only less than 2% to the buoyancy dissipation χ . The only statistic that is dominated by departures from the spanwise average is mechanical energy dissipation, ε , in the fourth column. Thus table 5 – particularly the third column – supports the view that the 3D Nu at $Ra = 3.20 \times 10^{11}$ is largely determined by the 2D spanwise averaged circulation.

Figure 11(a) shows that there is no inertial cascade in the interior of the **3DFS** solution. An inertial cascade is characterized by a kinetic energy spectrum $\sim \varepsilon^{2/3} k^{-5/3}$, or a vorticity spectrum $\sim \varepsilon^{2/3} k^{+1/3}$. The ultra-violet vorticity divergence is cut-off at a wavenumber of order η_K^{-1} , where $\eta_K \sim \delta_{1/4}$ is the Kolmogorov length. But the snapshot in figure 11(a) shows that the interior vorticity is concentrated on length scales very much larger than η_K . Instead of looking for signatures of 3D turbulence, it is informative to compare figure 11 with the corresponding **2DFS** run in figure 12.

The 2D vortices in figure 12(a) have larger length scale and are more intense than the 3D vorticity fluctuations in figures 11(a) and (c). The larger scale of the 2D vortices might result from vortex mergers occurring during the disintegration central plume. These mergers preserve vorticity extrema (Carnevale *et al.* 1991) so that strong vorticity from the BL – evident in figures 5 (c) and (d) – is carried into the interior.

The comparison of figure 11 with 12 indicates that there is no significant amplification of vorticity in the interior of the 3D solution. Indeed the interior vorticity is stronger in the 2D solution than in the 3D solution. Perhaps $Ra = 3.2 \times 10^{11}$ is far too small for turbulent activation of vortex stretching in the interior of HC? But we now show that significant 3D vorticity amplification cannot occur in HC even as $Ra \rightarrow \infty$. In other words, $\langle |\omega|^2 \rangle_{3D}$ is almost equal to $\langle |\omega|^2 \rangle_{2D}$ even as $Ra \rightarrow \infty$.

With a well known identity, the kinetic energy dissipation can be written as $\varepsilon = \nu \langle |\omega|^2 \rangle$

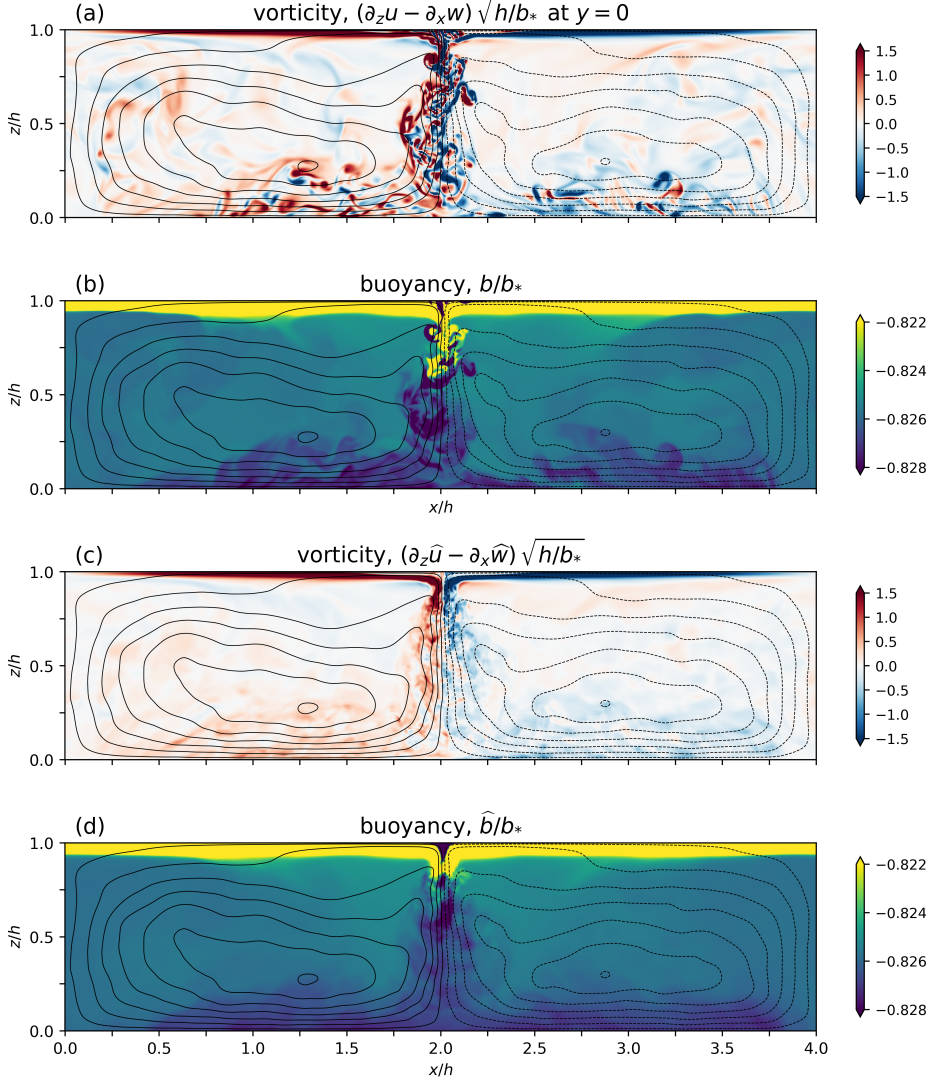


Figure 11: Panels (a) and (b) show a y -slice of snapshots of the 3DFS solution at $Ra = 3.20 \times 10^{11}$. The spanwise averages of the snapshots of vorticity and buoyancy are shown in panels (c) and (d). In all panels, the contours are streamlines computed from a spanwise averaged snapshot at the final time. At the top surface $-1 \leq b/b_* \leq +1$; the narrow range of the buoyancy color scale makes the small interior variations visible.

where $\omega = \nabla \times \mathbf{u}$ is the vorticity. Then the mechanical energy power integral (2.8) rewritten as

$$\frac{\langle |\omega|^2 \rangle}{b_\star/h} = -\frac{\kappa}{\nu} \frac{\bar{b}(0)}{b_\star}, \quad (7.1)$$

The left hand side of (7.1) is a nondimensional mean square vorticity. The result (7.1) is independent of ℓ_y/h and can be used to compare a 3D flow with a numerically accessible 2D “comparison flow” at the same Ra . This comparison produces the inequality

$$\frac{\langle |\omega|^2 \rangle_{2D}}{b_\star/h} \leq \frac{\langle |\omega|^2 \rangle_{3D}}{b_\star/h} \leq \frac{\kappa}{\nu}. \quad (7.2)$$

	$\langle \hat{\mathbf{u}} ^2 \rangle / \langle \mathbf{u} ^2 \rangle$	$\langle v^2 \rangle / \langle \mathbf{u} ^2 \rangle$	$\kappa \langle b_y^2 \rangle / \chi$	$v \langle \zeta^2 \rangle / \varepsilon$
3DFS	0.662	0.112	0.013	0.187
3DNS	0.690	0.092	0.019	0.342

Table 5: Statistics for the 3D solutions at $Ra = 3.20 \times 10^{11}$. The ratios above were computed from a single snapshot at the final time, i.e., without the benefit of time averaging. These ratios decrease monotonically to zero as Ra is lowered to the critical value for the onset of 3D motion. In the first column, $\hat{\mathbf{u}} = (-\psi_z, 0, \psi_x)$ is the spanwise averaged velocity in (4.4) and in the final column $\zeta = -\nabla^2 \psi$ is the vorticity of the spanwise-averaged flow.

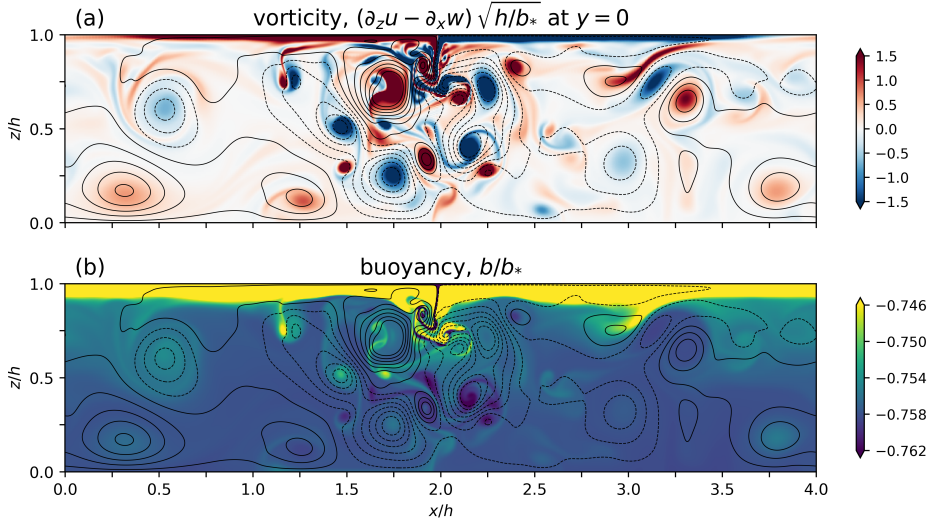


Figure 12: Snapshot of the 2DFS solution at $Ra = 3.20 \times 10^{11}$. The contours are streamlines. The narrow range of the buoyancy color scale makes the small interior variations visible.

The first \leqslant in (7.2) is because if to the contrary $\langle |\omega|^2 \rangle_{2D} > \langle |\omega|^2 \rangle_{3D}$ then there is no 3D vorticity amplification and the proof is finished. The second \leqslant in (7.2) follows from the buoyancy extremum principle $\bar{b}(0) \geqslant -b_\star$.

The 2D high Ra solutions found here already come close to meeting the buoyancy extremum bound. Therefore (7.2) tightly constrains $\langle |\omega|^2 \rangle_{3D}$ to a narrow range. For example, consider the implications of (7.2) using the $Ra = 6.4 \times 10^{13}$ 2DFS solution in figures 2(c) and (d) as a comparison flow. At $Ra = 6.4 \times 10^{13}$ the 3D flow is not accessible to direct numerical solution. But the 2D comparison solution has $\bar{b}_{2D}(0)/b_\star \approx -0.85$ and then (7.2) becomes

$$0.85 \frac{\kappa}{v} \leqslant \frac{\langle |\omega|^2 \rangle_{3D}}{b_\star/h} \leqslant \frac{\kappa}{v}, \quad \text{at } Ra = 6.4 \times 10^{13}. \quad (7.3)$$

Thus at $Ra = 6.4 \times 10^{13}$ the 3D flow has at most only 18% more mean square vorticity than that of the 2D comparison flow in figure 2(d).

With the argument above, numerical values of $\langle |\omega|^2 \rangle$ and bottom buoyancy $b(0)/b_\star$ obtained from 2D direct numerical solution can be leveraged to constrain $\langle |\omega|^2 \rangle$ of 3D HC flows at the same Ra . Moreover it is likely that as $Ra \rightarrow \infty$ the 2D solutions will come closer to meeting the extremum bound. In this case as $Ra \rightarrow \infty$, $\langle |\omega|^2 \rangle_{3D}$ in (7.2) is sandwiched into an ever narrower range and $\langle |\omega|^2 \rangle \rightarrow \kappa b_\star/vh$ for all values of ℓ_y/h .

In view of the controversial application of the zeroth law of turbulence to HC (Paparella & Young 2002; Scotti & White 2011; Shishkina *et al.* 2016) it is interesting that the efficacy of 3D HC vortex stretching is limited by the feeble supply of mechanical energy.

As a concluding illustration of $\langle |\omega|^2 \rangle \approx \kappa b_\star / vh$, notice that in figures 1 and 2 the vorticity is scaled with $\sqrt{b_\star/h}$ even as Ra is varied by a factor of 10^6 . Indeed this simple estimate of root mean square vorticity applies to all 2D and 3D solutions reported here, e.g., including the zoomed-in view of the BL in figure 5.

8. Conclusion

We have conducted a numerical study of the Ra - Nu relation with $Pr = 1$ and four cases corresponding to no-slip or free-slip boundary conditions, in both 2D ($\ell_y/h = 0$) and 3D ($\ell_y/h = 1$) geometries. In all four cases, with Ra in the range 10^6 to 10^{10} , we find that $Nu \sim Ra^{1/5}$. In the 2D cases, with maximum Rayleigh number of order 10^{14} , we find a scaling regime with $Nu \sim Ra^{1/4}$; see also Tsai *et al.* (2020).

The $Nu \sim Ra^{1/4}$ regime has a double boundary layer structure. There is a main boundary layer with thickness $\sim Ra^{-1/5}$ and an inner boundary layer with thickness $\sim Ra^{-1/4}$. The thickness of the inner boundary layer corresponds to the Kolmogorov–Batchelor scales of HC in (6.3).

Scaling arguments for the Nu - Ra relation of HC reviewed in section 4 do not depend very much, if at all, on the distinction between 2D and 3D HC. Nor do these arguments identify the spanwise aspect ratio ℓ_y/h as an important parameter. Thus it is informative to conduct parallel numerical studies of 2D and 3D HC and compare corresponding Nu 's. This comparison of 2D with 3D HC, extending to $Ra = 3.2 \times 10^{11}$, shows that 3D HC has only a slight 10% or 20% enhancement of heat transport over non-turbulent 2D HC. Boundary conditions are more important than dimensionality: the 2D free-slip solutions have larger Nu than 3D no-slip solutions at the same Ra .

The conclusions above are based on 3D computations with $Ra \leq 3.2 \times 10^{11}$ and geophysical Ra 's are larger by 10^{10} or 10^{12} . With the inequality (7.2), however, we can use results from 2D numerical solutions to constrain the mean square vorticity of 3D HC at the same Ra . With the additional plausible assumption that the bottom buoyancy of 2D solutions approaches that of the densest surface fluid, inequality (7.2) implies that in 2D and in 3D the mean square vorticity of HC limits to $\kappa b_\star / vh$ as $Ra \rightarrow \infty$. Thus vortex stretching and vorticity amplification do not operate in 3D HC. These results reinforce the view that 3D HC does not express all of the characteristics of turbulence.

Acknowledgments

Without implying their endorsement, we thank Basile Gallet, Ross Griffiths for discussions of horizontal convection. Computational resources were provided by the Australian National Computational Infrastructure at the Australian National University, which is supported by the Commonwealth of Australia. NCC was supported by the Australian Research Council DECRA Fellowship DE210100749. CBR was supported by National Aeronautics and Space Administration Award NNX16AO5OH. SGLS was partially supported by National Science Foundation Awards OCE-1829919. WRY was supported by National Science Foundation Awards OCE-1657041 and OCE-2048583.

Declaration of interests

The authors report no conflict of interest.

Appendix A. The low Rayleigh number regime

If the Rayleigh number is sufficiently small then one can employ a straightforward expansion in powers of Ra to show that the Nusselt number is

$$Nu = 1 + C_2 Ra^2 + \text{ord}(Ra^4). \quad (\text{A } 1)$$

In the expansion (A 1), C_2 is a function of the aspect ratio, $A_x = \ell_x/h$, but not the Prandtl number Pr . In this appendix we summarize the calculation of C_2 for horizontal convection forced with the sinusoidal b_s in (2.4). This calculation is more interesting than one might anticipate because C_2 turns out to be a very small number for all values of the aspect ratio A_x . Consequently with the aspect ratio $A_x = 4$ used in this work “sufficiently small” means Rayleigh numbers of order 10^4 (see the inset in figure 4).

Using the streamfunction formulation, with $(u, w) = (-\psi_z, \psi_x)$, and scaling lengths with the depth h and time with h^2/κ the steady Boussinesq equations are

$$\psi_x \nabla^2 \psi_z - \psi_z \nabla^2 \psi_x = b_x + Pr \nabla^4 \psi, \quad (\text{A } 2)$$

$$\psi_x b_z - \psi_z b_x = \nabla^2 b, \quad (\text{A } 3)$$

where here $\nabla^2 = \partial_x^2 + \partial_z^2$ is the two-dimensional Laplacian; the spanwise vorticity is $u_z - w_x = -\nabla^2 \psi$. The surface boundary condition is $b(x, 1) = \epsilon \cos mx$ where

$$m \stackrel{\text{def}}{=} kh = 2\pi/A_x, \quad \text{and} \quad \epsilon \stackrel{\text{def}}{=} PrRa/A_x^3 = PrRa(m/2\pi)^3. \quad (\text{A } 4)$$

We expand all variables in powers of the small parameter ϵ

$$(b, \psi) = \epsilon(b_1, \psi_1) + \epsilon^2(b_2, \psi_2) + \dots \quad (\text{A } 5)$$

The first-order equations are

$$Pr \nabla^4 \psi_1 = -b_{1x}, \quad \text{and} \quad \nabla^2 b_1 = 0. \quad (\text{A } 6)$$

The solution (A 6) is

$$\psi_1 = \sin mx P(z), \quad \text{and} \quad b_1 = \cos mx B(z), \quad (\text{A } 7)$$

where $B(z) \stackrel{\text{def}}{=} \operatorname{sech} m \cosh mz$. In $\psi_1(x, z)$ we have the free-slip function

$$P^{\text{FS}}(z) = \frac{B(z)}{8m^2 Pr} [(m \coth m + 1 - z) \tanh mz - mz(2 - z)], \quad (\text{A } 8)$$

and the no-slip function

$$P^{\text{NS}}(z) = \frac{1}{8m Pr (\sinh^2 m - m^2)} \left[(\sinh^2 m - m^2)(z^2 - z)B(z) + (\tanh m - m)z \sinh m(1 - z) + (\sinh m - m \operatorname{sech} m)(1 - z) \sinh mz \right]. \quad (\text{A } 9)$$

At second order in ϵ we must solve

$$\nabla^2 b_2 = \psi_{1x} b_{1z} - \psi_{1z} b_{1x}, \quad (\text{A } 10)$$

$$= \underbrace{\frac{1}{2}m(PB)' + \frac{1}{2}m(PB' - P'B)}_{J_0} \cos 2mx + \underbrace{\frac{1}{2}m(PB' - P'B)}_{J_2} \cos 2mx. \quad (\text{A } 11)$$

The solution of (A 11) has the form

$$b_2 = B_{20}(z) + B_{22}(z) \cos 2mx, \quad (\text{A } 12)$$

where B_{20} and B_{22} are determined by solving

$$B''_{20} = J_0, \quad (\text{A } 13)$$

$$B''_{22} - 4m^2 B_{22} = J_2. \quad (\text{A } 14)$$

Forming $\langle B_{22}(\text{A } 14) \rangle$ we find the shortcut used below in passing from (A 16) to (A 17):

$$\left\langle B'_{22}^2 + 4m^2 B_{22}^2 \right\rangle = -\langle B_{22} J_2 \rangle. \quad (\text{A } 15)$$

The expressions for B_{22} and B_{20} , obtained with Mathematica, are complicated and are not explicitly presented. Mercifully, to obtain the coefficient C_2 in (A 1), we do not need ψ_2 .

Multiplying $\nabla^2 b_1 = 0$ by b_n , with $n \geq 2$, and noting that all these b_n 's have homogeneous boundary conditions at $z = 0$ and 1, we see that $\langle \nabla b_n \cdot \nabla b_1 \rangle = 0$. Consequently the expansion of the buoyancy variance dissipation is

$$\chi = \underbrace{\epsilon^2 \langle |\nabla b_1|^2 \rangle}_{\chi_2 = \frac{1}{2} m \tanh m} + \underbrace{\epsilon^4 \langle |\nabla b_2|^2 \rangle}_{\chi^4} + \text{ord}(\epsilon^6). \quad (\text{A } 16)$$

Recalling the definition of ϵ in (A 4), the Nusselt number is

$$Nu = 1 + \underbrace{\frac{m^2 \langle (PB)^2 \rangle - 2\langle B_{22} J_2 \rangle}{2m \tanh m}}_{\chi^4/\chi_2} \left(\frac{m^3 Pr}{8\pi^3} \right)^2 Ra^2 + \dots. \quad (\text{A } 17)$$

Because P , B_{22} , and J_2 are all proportional to Pr^{-1} , the Prandtl number Pr cancels out of the coefficient of Ra^2 in (A 17).

With FS boundary conditions, the expression for C_2 in (A 1) is

$$C_2^{FS} = \left[690 - 1920m^4 \operatorname{cosech}^2 m + 20(3 + 4m^2)^2 \operatorname{sech} 2m \right. \\ \left. + m(1024m^4 - 80m^2 - 6195) \operatorname{cosech} m \operatorname{sech}^3 m \right. \\ \left. + 5(352m^4 - 624m^2 + 1065) \operatorname{sech}^2 m \right] / 41\,943\,040\,\pi^6. \quad (\text{A } 18)$$

Limiting values in the FS case are

$$\lim_{m \rightarrow 0} C_2^{FS} = \frac{31m^8}{30\,965\,760\pi^6} + \text{ord}(m^{10}), \quad (\text{A } 19)$$

and

$$\lim_{m \rightarrow \infty} C_2^{FS} = \frac{69}{4\,194\,304\,\pi^6}. \quad (\text{A } 20)$$

We admire the frequently occurring integer $4\,194\,304 = 2^{22}$ in the formulas above and below.

With NS boundary conditions, we find

$$C_2^{NS} = \frac{1}{41\,943\,040\,\pi^6} \frac{\Xi(m)}{(\cosh 2m - 2m^2 - 1)^2}, \quad (\text{A } 21)$$

where

$$\begin{aligned}
 \Xi(m) = & 85 \cosh 4m - 320m(33 + 8m^2) \sinh 2m + 10(845 + 716m^2) \cosh 2m \\
 & - 5(5123 + 18304m^2 + 13720m^4 + 2912m^6) \\
 & - 4m^5(7215 + 100m^2 - 64m^4) \coth m \\
 & + 20(829 + 4402m^2 + 5289m^4 + 836m^6 - 64m^8) \operatorname{sech}^2 m \\
 & - 4m(4785 + 8010m^2 + 1549m^4 - 212m^6 + 64m^8) \tanh m \operatorname{sech}^2 m \\
 & + 20(25 - 184m^2 - 80m^4 - 16m^6) \operatorname{sech} 2m \\
 & + 4m(8865 + 21640m^2 + 17719m^4 + 740m^6 - 64m^8) \tanh m \\
 & + 160m(15 - 7m^2 - 4m^4) \tanh 2m. \tag{A 22}
 \end{aligned}$$

Limiting values in the **NS** case are

$$\lim_{m \rightarrow 0} C_2^{\textcolor{red}{NS}} = \frac{m^8}{30\,965\,760\pi^6} + \operatorname{ord}(m^{10}), \tag{A 23}$$

and

$$\lim_{m \rightarrow \infty} C_2^{\textcolor{red}{NS}} = \frac{17}{4\,194\,304\pi^6}. \tag{A 24}$$

It is notable that the small- m $C_2^{\textcolor{red}{NS}}$ in (A 23) is smaller by a factor of exactly 31 than $C_2^{\textcolor{blue}{FS}}$ in (A 19).

Both C_2 's are very much less than one for all aspect ratios. In the numerical solutions summarized in figure 4, the aspect ratio is $A_x = 4$, corresponding to $m = kh = \pi/2$. The results in (3.3) and (3.4) follow by evaluating the formulas (A 18) through (A 22) with $m = \pi/2$.

REFERENCES

- BENZI, R., PATARNELLO, S & SANTANGELO, P 1987 On the statistical properties of two-dimensional decaying turbulence. *Europhys. Lett.* **3** (7), 811.
- BENZI, R., PATARNELLO, S & SANTANGELO, P 1988 Self-similar coherent structures in two-dimensional decaying turbulence. *J. Phys. A* **21** (5), 1221.
- BURNS, K. J., VASIL, G. M., OISHI, J. S., LECOANET, D. & BROWN, B. P. 2020 Dedalus: A flexible framework for numerical simulations with spectral methods. *Phys. Rev. Res.* **2**, 023068.
- CARNEVALE, G. F., MCWILLIAMS, J. C., POMEAU, Y., WEISS, J. B. & YOUNG, W. R. 1991 Evolution of vortex statistics in two-dimensional turbulence. *Phys. Rev. Lett.* **66** (21), 2735.
- CHIU-WEBSTER, S., HINCH, E. J. & LISTER, J. R. 2008 Very viscous horizontal convection. *J. Fluid Mech.* **611**, 395–426.
- COMAN, M. A., GRIFFITHS, R. W. & HUGHES, G. O. 2006 Sandström's experiments revisited. *J. Mar. Res.* **64** (6), 783–796(14).
- DRITSCHEL, D. G., SCOTT, R. K., MACASKILL, C., GOTZWALD, G. A. & TRAN, C. V. 2008 Unifying scaling theory for vortex dynamics in two-dimensional turbulence. *Phys. Rev. Lett.* **101** (9), 094501.
- GAYEN, B., GRIFFITHS, R. W. & HUGHES, G. O. 2014 Stability transitions and turbulence in horizontal convection. *J. Fluid Mech.* **751**, 698–724.
- HUGHES, G. O. & GRIFFITHS, R. W. 2008 Horizontal convection. *Annu. Rev. Fluid Mech.* **40**, 185–208.
- ILICAK, M. & VALLIS, G. K. 2012 Simulations and scaling of horizontal convection. *Tellus A* **64** (1), 18377.
- MCWILLIAMS, J. C. 1984 The emergence of isolated, coherent vortices in turbulent flow. *J. Fluid Mech.* **146**, 21–43.
- MCWILLIAMS, J. C. 1990 The vortices of two-dimensional turbulence. *J. Fluid Mech.* **219**, 361–385.
- MULLARNEY, J. C., GRIFFITHS, R. W. & HUGHES, G. O. 2004 Convection driven by differential heating at a horizontal boundary. *J. Fluid Mech.* **516**, 181–209.
- PAPARELLA, F. & YOUNG, W. R. 2002 Horizontal convection is non-turbulent. *J. Fluid Mech.* **466**, 205–214.

- PASSAGGIA, PIERRE-YVES, SCOTTI, ALBERTO & WHITE, BRIAN 2017 Transition and turbulence in horizontal convection: linear stability analysis. *J. Fluid Mech.* **821**, 31–58.
- RAMME, LENNART & HANSEN, ULRICH 2019 Transition to time-dependent flow in highly viscous horizontal convection. *Physical Review Fluids* **4** (9), 093501.
- REITER, PHILIPP & SHISHKINA, OLGA 2020 Classical and symmetrical horizontal convection: detaching plumes and oscillations. *J. Fluid Mech.* **892**.
- ROCHA, C. B., BOSSY, T., LLEWELLYN SMITH, S. G. & YOUNG, W. R. 2020a Improved bounds on horizontal convection. *J. Fluid Mech.* **883**, A41.
- ROCHA, C. B., CONSTANTINOU, N. C., LLEWELLYN SMITH, S. G. & YOUNG, W. R. 2020b The Nusselt numbers of horizontal convection. *J. Fluid Mech.* **894**, A24.
- ROSSBY, H. T. 1965 On thermal convection driven by non-uniform heating from below: an experimental study. *Deep Sea Res.* **12** (1), 9–10, IN9–IN14, 11–16.
- ROSSBY, H. T. 1998 Numerical experiments with a fluid heated non-uniformly from below. *Tellus A* **50** (2), 242–257.
- SANDSTRÖM, J. W. 1908 Dynamische versuche mit meerwasser. *Annals in Hydrodynamic Marine Meteorology* **36**, 6–23.
- SCOTTI, A. & WHITE, B. 2011 Is horizontal convection really “non-turbulent”?”. *Geophys. Res. Lett.* **38** (21), L21609.
- SHEARD, G. J. & KING, M. P. 2011 Horizontal convection: effect of aspect ratio on Rayleigh number scaling and stability. *Appl. Math. Modelling* **35** (4), 1647–1655.
- SHISHKINA, O., GROSSMANN, S. & LOHSE, D. 2016 Heat and momentum transport scalings in horizontal convection. *Geophys. Res. Lett.* **43** (3), 1219–1225.
- SHISHKINA, OLGA & WAGNER, SEBASTIAN 2016 Prandtl-number dependence of heat transport in laminar horizontal convection. *Physical Review Letters* **116** (2), 024302.
- SIGGERS, J. H., KERSWELL, R. R. & BALMFORTH, N. J. 2004 Bounds on horizontal convection. *J. Fluid Mech.* **517**, 55–70.
- TSAI, T., HUSSAM, W. K., FOURAS, A. & SHEARD, G. J. 2016 The origin of instability in enclosed horizontally driven convection. *Int. J. Heat and Mass Transfer* **94**, 509–515.
- TSAI, T., HUSSAM, W. K., KING, M. P. & SHEARD, G. J. 2020 Transitions and scaling in horizontal convection driven by different temperature profiles. *Int. J. Thermal Sci.* **148**, 106166.
- WANG, W. & HUANG, R. X. 2005 An experimental study on thermal convection driven by horizontal differential heating. *J. Fluid Mech.* **540**, 49–73.
- WINTERS, K. B. & YOUNG, W. R. 2009 Available potential energy and buoyancy variance in horizontal convection. *J. Fluid Mech.* **629**, 221–230.